nature communications

Article

https://doi.org/10.1038/s41467-024-53937-4

Rationally designed multimeric nanovaccines using icosahedral DNA origami for display of SARS-CoV-2 receptor binding domain

Received: 25 October 2023

Accepted: 28 October 2024

Published online: 06 November 2024

Check for updates

Qingqing Feng[1,2,3,7], Keman Cheng[1,2,3,7], Lizhuo Zhang[1,2,3,7], Dongshu Wang[4,7], Xiaoyu Gao[1,2,3], Jie Liang[1,2,3], Guangna Liu[1,2,3], Nana Ma[1,2,3], Chen Xu[1,2,3], Ming Tang[1,2,3], Liting Chen[1,2,3], Xinwei Wang[1,2,3], Xuehui Ma[5], Jiajia Zou[6], Quanwei Shi[6], Pei Du[5], Qihui Wang[5], Hengliang Wang[4] ✉, Guangjun Nie[1,2] ✉ & Xiao Zhao[1,2,3] ✉

Multivalent antigen display on nanoparticles can enhance the immunogenicity of nanovaccines targeting viral moieties, such as the receptor binding domain (RBD) of SARS-CoV-2. However, particle morphology and size of current nanovaccines are significantly different from those of SARS-CoV-2. Additionally, surface antigen patterns are not controllable to enable the optimization of B cell activation. Herein, we employ an icosahedral DNA origami (ICO) as a display particle for RBD nanovaccines, achieving morphology and diameter like the virus (91 ± 11 nm). The surface addressability of DNA origami permits facile modification of the ICO surface with numerous RBD antigen clusters (ICO-RBD) to form various antigen patterns. Using an in vitro screening system, we demonstrate that the antigen spacing, antigen copies within clusters and cluster number parameters of the surface antigen pattern all impact the ability of the nanovaccines to activate B cells. Importantly, the optimized ICO-RBD nanovaccines evoke stronger and more enduring humoral and T cell immune responses in female mouse models compared to soluble RBD antigens, and the multivalent display broaden the protection range of B cell responses to more mutant strains. Our vaccines activate similar humoral immunity, observable stronger cellular immunity and more memory immune cells compared to trimeric mRNA vaccines.

The global coronavirus pandemic caused by the severe acute respiratory syndrome coronavirus 2 (SARS-CoV-2), has profoundly affected human health[1]. Several types of vaccines fabricated via differing technological routes were developed to combat the coronavirus disease 2019 (COVID-19) pandemic caused by SARS-CoV-2[2,3]. Among them, the subunit vaccines that comprise only key viral proteins have become the most widely successful SARS-CoV-2 vaccine candidates, in both clinical and preclinical stages, due to their well-characterized ingredients and favorable safety[4–6]. The receptor binding domain (RBD) in the surface spike (S) protein of SARS-CoV-2 is the dominant domain for the interaction between viruses and human cells, which makes this subunit the most attractive vaccine epitope target because it elicits functionally neutralizing antibodies to block virus invasion, avoiding the potential risk of

A full list of affiliations appears at the end of the paper. ✉e-mail: wanghl@bmi.ac.cn; niegj@nanoctr.cn; zhaox@nanoctr.cn

antibody-dependent enhancement due to non-neutralizing antibodies[7–9].

To date, several subunit vaccines targeting SARS-CoV-2 RBD have been approved or entered clinical trials. Although there have been seminal reports about RBD monomer vaccines[10,11], the low molecular weight and surface valence limit their immunogenicity. RBD multimerization, such as dimerization via Fc fragment fusion or disulfide bonding and trimerization via stabilization by the T4 fibritin foldon domain, is a popular and useful strategy to overcome these drawbacks[12–16]. Recently, to further improve antigen size and surface valence, the method of displaying multiple copies of RBD on nanoparticles has received increasing attention. Nanoparticles with highly repetitive surface patterns, such as virus-like particles and ferritin, have been employed to establish multimeric RBD nanovaccines to improve the lymph node drainage of antigens and promote the ability to induce B cell receptor (BCR) crosslinking and activation[17–19]. However, the sizes of these nanovaccines (10–30 nm) are significantly smaller than that of SARS-CoV-2 (~ 90 nm), and the surface antigen patterns differ from the cluster distribution in SARS-CoV-2[20–23]. Nanoparticles with controllable dimensional morphologies and surface patterns are required to improve the similarity between RBD nanovaccines and SARS-CoV-2 and to explore the structure-activity relationship between surface antigen pattern and vaccine efficacy.

As a type of DNA nanotechnology, DNA origami entails the combination of one or more template strands with numerous staple strands, which together self-assemble via complementary base pairing[24]. Due to the precise controllability of DNA strands, DNA origami is morphologically programmable and can be assembled into nanostructures with different sizes and morphologies[25,26]. In addition, DNA origami possesses surface addressability because of the specificity of DNA sequences; the staple strands in DNA origami can be designed as capture strands, through sequence elongation and end modification, for subsequent molecular linkage with controllable spacing, number and pattern[25]. Due to these characteristics, DNA origami has become an ideal tool to study the relationship between the spatial arrangement and biological function of proteins, such as enzymes, receptors/ligands and antibodies, at the nanoscale[27–30]. Importantly, nanoscale antigen organization has been proven to affect B cell activation[31]. Additionally, the surface pattern of RBD distribution is associated with SARS-CoV-2 infection ability[32]. Therefore, using DNA origami to build biomimetic nanovaccines with similar sizes and surface antigen patterns to the corresponding viruses, such as SARS-CoV-2, may facilitate the development of highly effective antiviral vaccines.

Although there were several studies about the SARS-CoV-2 nanovaccines based on the DNA origami scaffolds, the structure-activity relationship between surface antigen pattern and vaccine efficacy was still elusive, and the underlying mechanism of those immune effects in vivo has not been scrutinized[33,34]. In the present study, we employed DNA origami to rationally design and precisely assemble RBD nanovaccines against SARS-CoV-2. We first constructed an icosahedral DNA origami (ICO) of ~90 nm in diameter, which approximated the morphology and size of SARS-CoV-2 (Fig. 1a). We then generated various surface antigen patterns with different parameters, including antigen spacing, antigen copies within clusters and cluster numbers, and precisely decorated RBD antigens onto ICO (ICO-RBD) using an "engraving-printing" strategy (Fig. 1a). In vitro experiments using B cells stably expressing the RBD antigen's cognate IgG receptor were performed to interrogate the impacts of these parameters on B cell activation and screen for nanovaccines with optimal surface RBD patterns (Fig. 1b). Finally, we systematically evaluated the short- and long-term immune effects of the optimized ICO-RBD nanovaccines in mouse models and compared the immune effects of the nanovaccines with trimeric mRNA vaccines (Fig. 1b).

Results and discussion

Design and construction of ICO-RBD nanovaccines

The ICO was assembled by slowly annealing the genomic DNA of M13mp18 bacteriophage as a template strand together with multiple staple and capture strands (Supplementary Data 1). In observation using negative staining transmission electron microscopy (TEM) and atomic force microscopy (AFM), ICO exhibited a uniform, hollowed-out polyhedron structure of ~80–90 nm in diameter (Fig. 1c, d). The hydrophilic diameter of ICO was 93 nm, as detected using dynamic light scattering (DLS; Fig. 1e), which is close to that of SARS-CoV-2. We also verified the successful assembly of ICO according to migration in agarose gel electrophoresis, compared to the genomic DNA of M13mp18 bacteriophage (Fig. 1f). In addition, ICO exhibited high stability property under 20% fetal bovine serum (FBS) up to 24 h (Fig. 1f), which is favorable to stimulate immune cells in vivo.

Next, we adopted an "engraving-printing" strategy to decorate prototype RBD antigens onto ICO (Fig. 1a). In brief, the 5′-ends of staple strands at predetermined positions were elongated with overhanging polyA to form capture strands. The polyA overhang did not interfere with origami assembly, even if the number of capture strands increased to 60 (Supplementary Fig. 1a). Next, the C-terminal azide-modified SpyTag peptide glue (SpyTag-N3) and 5′-end dibenzocyclooctyne (DBCO)-modified polyT (DBCO-polyT) were covalently linked through click chemistry to form SpyTag-polyT conjugates. Next, we "engraved" ICO with the SpyTag peptides through DNA complementary hybridization between the polyT in the SpyTag-polyT conjugates and the polyA overhang in the capture strands (Supplementary Fig. 1b). Finally, fusion proteins of SpyCatcher and RBD (N-SpyCatcher-RBD-C; Supplementary Fig. 2a–c) were "printed" onto ICO through the spontaneous covalent isopeptide bond formation between SpyCatcher and SpyTag[35], ultimately achieving site-specific decoration of RBD antigens onto the surface of ICO. We designed and constructed 5 different ICO-RBD nanovaccines surface-modified with 12, 24, 36, 48 or 60 RBD antigens. As the number of modified RBD antigens increased, the electrophoretic migration of ICO-RBD decreased (Fig. 1g), indicating successful protein decoration of the nanoparticles. By measuring the DNA and protein concentration, we show that the loading efficiency of RBD antigens in ICO-RBD reached greater than 85% when the number of RBD antigens increased from 12 to 60 (Fig. 1h). This high efficiency is attributed to the mild conditions and rapid reaction kinetics of the click chemistry reaction and peptide glue technology. In addition, the site-specific conjugation based on the peptide glue technology ensured a uniform outward orientation of RBD antigens on the ICO-RBD nanovaccines, which is beneficial to the antigenic immune stimulation of B cells. Also, the SpyCatcher-RBD proteins is obtained by fusion expression without any other chemical processing or modification, which fully guarantees their function and structure. In a word, the "engraving-printing" strategy exhibits high connection efficiency, ensures RBD connection direction and function itself. Further, the construction of programmed temperature control system can realize the scale-up production of DNA origami-based nanovaccine carriers, through the pre-design and assembly of rapidly synthesized DNA strands. Subsequently, the surface site-specific antigen modification can be performed through the mature protein purification technology and the efficient "engraving-printing" strategy, which is also conducive for scale-up production.

The size and shape of nanostructure correlates with their lymph node drainage in the body, which may determine the humoral immune response and the germinal center response[36]. Herein, based on genomic DNA of M13mp18 bacteriophage as a template strand, we designed octahedral DNA origami with about 28 nm diameter, icosahedral DNA origami with about 43 nm or 90 nm diameter. Then, using our "engraving-printing" strategy, five RBD proteins were displayed on their surface to form OCTA (~ 28 nm)-5 RBD, ICO (~ 43 nm)-5 RBD and

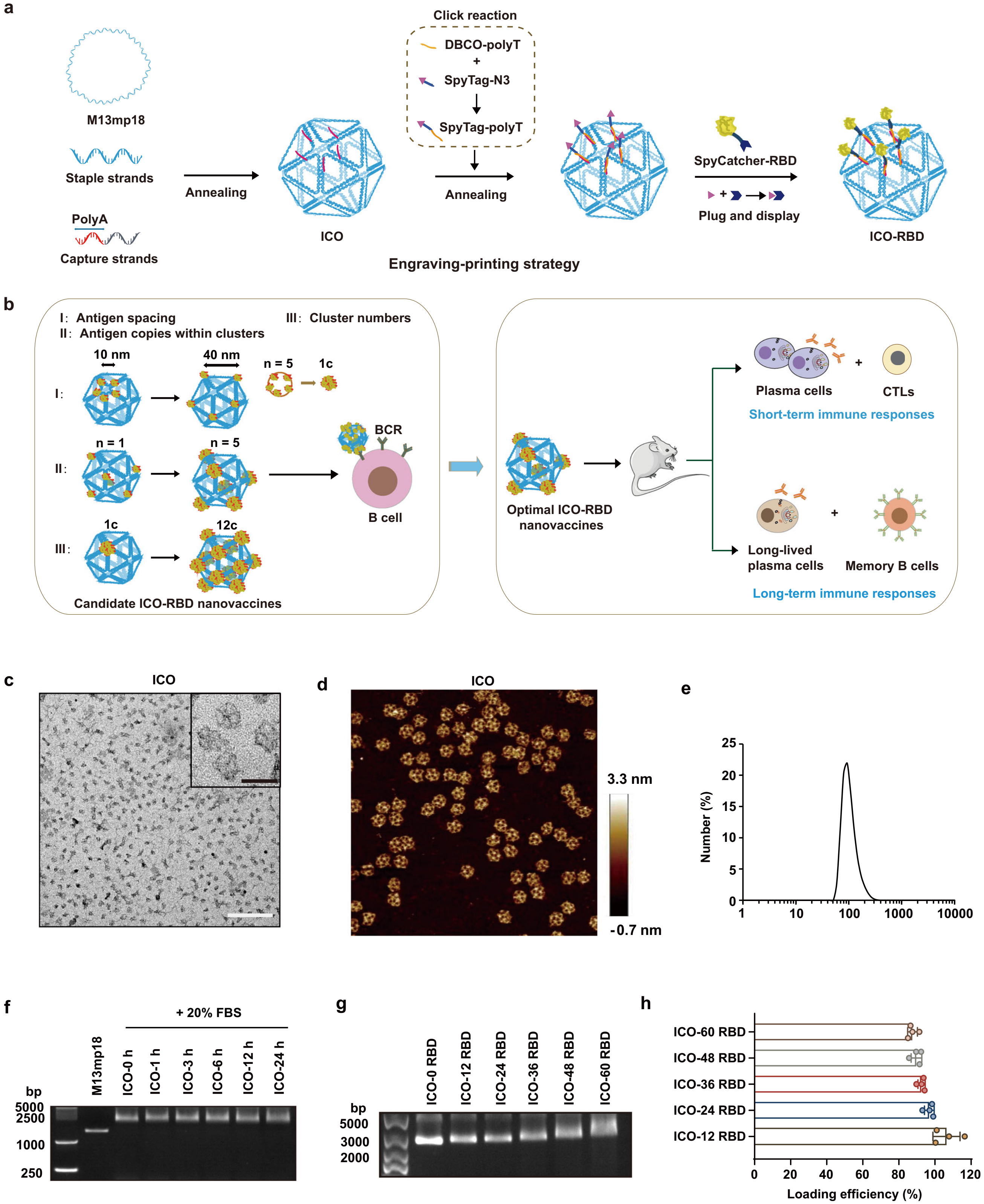

ICO (~90 nm)-5 RBD, respectively, to explore the effect of morphology on their antigen delivery capacity. The corresponding multiple staple and capture strands were showed in Supplementary Data 1. Free RBD monomer and RBD dimer were used as controls, and Cy5.5 was used to label these vaccines. These vaccines were given to mice by intramuscular injection, and the inguinal lymph nodes were isolated after different time intervals (up to 14 days). As shown in Supplementary Fig. 3a, compared to other vaccines, ICO (~90 nm)-5 RBD nanovaccines exhibited an improved accumulation in the inguinal lymph nodes. Further flow cytometry analysis showed that there were more Cy5.5$^+$ cells in DCs (CD11C$^+$), follicular DCs (CD21/CD35$^+$CD11C$^+$), resident DCs (CD103$^-$CD11C$^+$) and macrophages (F4/80$^+$) in the ICO (~90 nm)-5 RBD group than those in other groups (Supplementary Fig. 3b–f). These results reveal the excellent antigen delivery capability

Fig. 1 | Design and construction of ICO-RBD nanovaccines. **a** Schematic illustration of the "engraving-printing" strategy to decorate RBD antigens onto ICO. The genomic DNA of M13mp18 bacteriophage was annealed and folded together with staple and capture strands (with polyA overhangs) to form the ICO nanocore. The SpyTag-N3 and DBCO-polyT were covalently linked through click chemistry to form the SpyTag-polyT conjugates. Next, the SpyTag peptides were engraved onto ICO through hybridization between polyT and polyA. The fusion proteins, SpyCatcher-RBD (prototype), were printed onto ICO through the spontaneous covalent isopeptide bond formation between SpyCatcher and SpyTag. **b** Schematic illustration of the optimization screening of surface antigen patterns based on the efficiency of the nanovaccines to activate RBD-specific IgG-BCR in vitro and the evaluation of efficient short- and long-term immune responses in vivo. Various surface antigen patterns with different parameters, including antigen spacing (10–40 nm), antigen copies within clusters (1–5) and cluster numbers (1–12), were screened. Characterization of ICO, including TEM (**c**), AFM (**d**) and DLS ($n = 3$ independent experiments) (**e**) analysis. Scale bar (white), 1 μm. Scale bar (black), 100 nm. **f** Gel electrophoresis of genomic DNA of M13mp18 bacteriophage and ICO after incubation in 20% FBS for different time. Gel electrophoresis (**g**) and loading efficiency of ICO-RBD nanovaccines surface-modified with 12, 24, 36, 48 or 60 RBD antigens ($n = 4$ independent experiments) (**h**). These experiments (**c**, **d**, **f**, **g**) were repeated three times independently with similar results. The data were processed on GraphPad Prism 8 and are presented as the mean ± SD. Source data are provided as a Source Data file.

of 90 nm icosahedral DNA origami as nanocarriers, which we used as antigen carriers in subsequent experiments.

Differential efficacy of ICO-RBD nanovaccines with different surface antigen patterns on B cell activation

Next, we investigated the relationship between nanovaccine surface antigen pattern and B cell activation efficiency. We designed the surface RBD patterns in ICO-RBD nanovaccines in consideration of the cluster distribution features of RBD antigens in SARS-CoV-2. The precise control afforded by the DNA origami scaffold enabled us to fabricate ICO-RBD nanovaccines with varying antigen spacing, antigen copy number within clusters and cluster numbers. We termed the different ICO-RBD nanovaccines ICO-RBD-xc×n-d nm, in which xc represents cluster number, n represents antigen copy number within clusters and d represents the antigen spacing within clusters. To assess the capacity of the nanovaccines to activate B cells, we generated B cells that express BCRs with the RBD-targeting monoclonal neutralizing antibody COVA2-15 (B-RBD cells), as previously described[37,38], and assessed the cell binding and Ca^{2+} influx induced by the different ICO-RBD nanovaccines in vitro.

We began with ICO-RBD nanovaccines with only 1 RBD cluster of 5 RBD copies within the cluster, but with different RBD spacing from 10 to 40 nm (Fig. 2a and Supplementary Fig. 4a, b). With decreased RBD spacing, the affinity between the ICO-RBD nanovaccines and B-RBD cells gradually increased (Fig. 2b). The ability of ICO-RBD nanovaccines to trigger Ca^{2+} influx of B-RBD cells also negatively correlated with the RBD spacing (Fig. 2c). When the RBD spacing reached 40 nm, the ability of ICO-RBD nanovaccines to activate Ca^{2+} influx of B-RBD cells was similar with that of soluble RBD monomers (Fig. 2c). These results indicate that antigen clustering indeed enhances B cell activation over soluble RBD monomers, while the strongest B cell activation occurred under close antigen spacing. When the antigen spacing increases past a critical threshold, the RBD antigens lose their clustered characteristic.

We next sought to define the impact of antigen cluster number in ICO-RBD nanovaccines on B cell activation. To this end, we fixed the number of antigen copies within clusters at 5 and the antigen spacing at 10 nm, while altering the cluster number from 1 to 12 (Fig. 2d and Supplementary Fig. 4c, d). As shown in Fig. 2e, increasing the antigen cluster number improved the binding capacity between ICO-RBD nanovaccines and B-RBD cells. When the antigen cluster number reached 6, the binding ability became saturated, as indicated by the similar B cell binding of ICO-RBD-6c × 5–10 nm and ICO-RBD-12c × 5-10 nm. In the ICO-RBD nanovaccines with different antigen cluster numbers, ICO-RBD-6c × 5–10 nm was also the most effective at activating Ca^{2+} influx in B-RBD cells (Fig. 2f). This observation is also supported by the literature[23], in which it has been reported that a surface multi-cluster pattern similar to that on the surface of SARS-CoV-2 is beneficial for immune stimulation.

To further investigate the role of antigen copy number within the clusters on B cell response, we programmed several ICO-RBD-6c × n-10 nm nanovaccines with 1 to 5 antigen copies within clusters (Supplementary Figs. 4e, f and 5a). As shown in Supplementary Fig. 5b, c, the cluster antigen copy number was also an important factor for the immune stimulation ability of ICO-RBD nanovaccines. Interestingly, although it possessed the same number of antigens as SARS-CoV-2, the ICO-RBD-6c × 3-10 nm nanovaccine with 3 antigen copies within clusters was not the most effective formulation; nanovaccine efficacy continued to improve as cluster antigen copy number increased, demonstrating the importance of rational artificial vaccine design. In summary, through screening and functional evaluation, the ICO-RBD-6c × 5–10 nm nanovaccine was the optimal ICO-RBD preparation. We chose these parameters for the subsequent in vivo experiments.

As for the structure-function relationship between antigen configuration and immunogenicity, our results are different from a previous study, in which the B cell activation decreased with increased spacing in the HIV antigen eOD-GT8[31]. The optimal surface antigen pattern maybe related to the type of virus antigens, indicating the importance of optimizing the surface antigen pattern during nanovaccine design. Here, considering the aggregation distribution of RBD antigen in SARS-CoV-2, we independently explored the relative effects of antigen spacing, antigen copies within clusters and cluster numbers on B cell activation based on DNA origami scaffold. We observed the closer the antigenic interval (~10 nm), the proximity in this distance may induce enhanced of B cells activation, which may be attributed to the polymeric effect when the antigen spacing is close enough and the antigen is displayed almost in the form of "clusters". In parallel, this observation further was supported that the pattern of multiple clusters on the surface of SARS-CoV-2 was beneficial to B cell stimulation. However, this enhancement stimulation is limited, and this activation reached a state of near saturation when the number of antigen aggregations increases to 6 clusters. Furthermore, when the antigen copies within each cluster increases or decreases, the polymer effect of the "cluster" will be enhanced or weakened or even disappear, showing either enhanced or diminished B-cell activation effects. For example, when the copy number is reduced to only 1, the RBD antigens lose their clustered characteristic and the polymer effect. The current results also show that the three copy within each cluster similar to those in natural structures are not the optimal, which illustrates the importance of artificial design.

Robust humoral immune responses induced by ICO-RBD nanovaccines in vivo

To assess the immunogenicity of ICO-RBD nanovaccines in vivo, we immunized 6-week-old BALB/c mice with two intramuscular injections of different ICO-RBD nanovaccines, containing 1 μg equivalent prototype RBD proteins, formulated with AddaVax adjuvant[6] (Fig. 3a). Phosphate buffered saline (PBS), RBD monomers (SpyCatcher-RBD proteins), ICO and RBD + ICO (physical mixture) were used as controls. As evaluated by enzyme-linked immunosorbent assay (ELISA), the serum titers of SARS-CoV-2 RBD-specific immunoglobulin G (IgG) in the RBD and ICO-RBD-6c × 5–10 nm groups reached 148 and 1738, respectively, 2 weeks after the priming immunization (Fig. 3b). After the boost immunization (given at week 3), the RBD-specific IgG titers

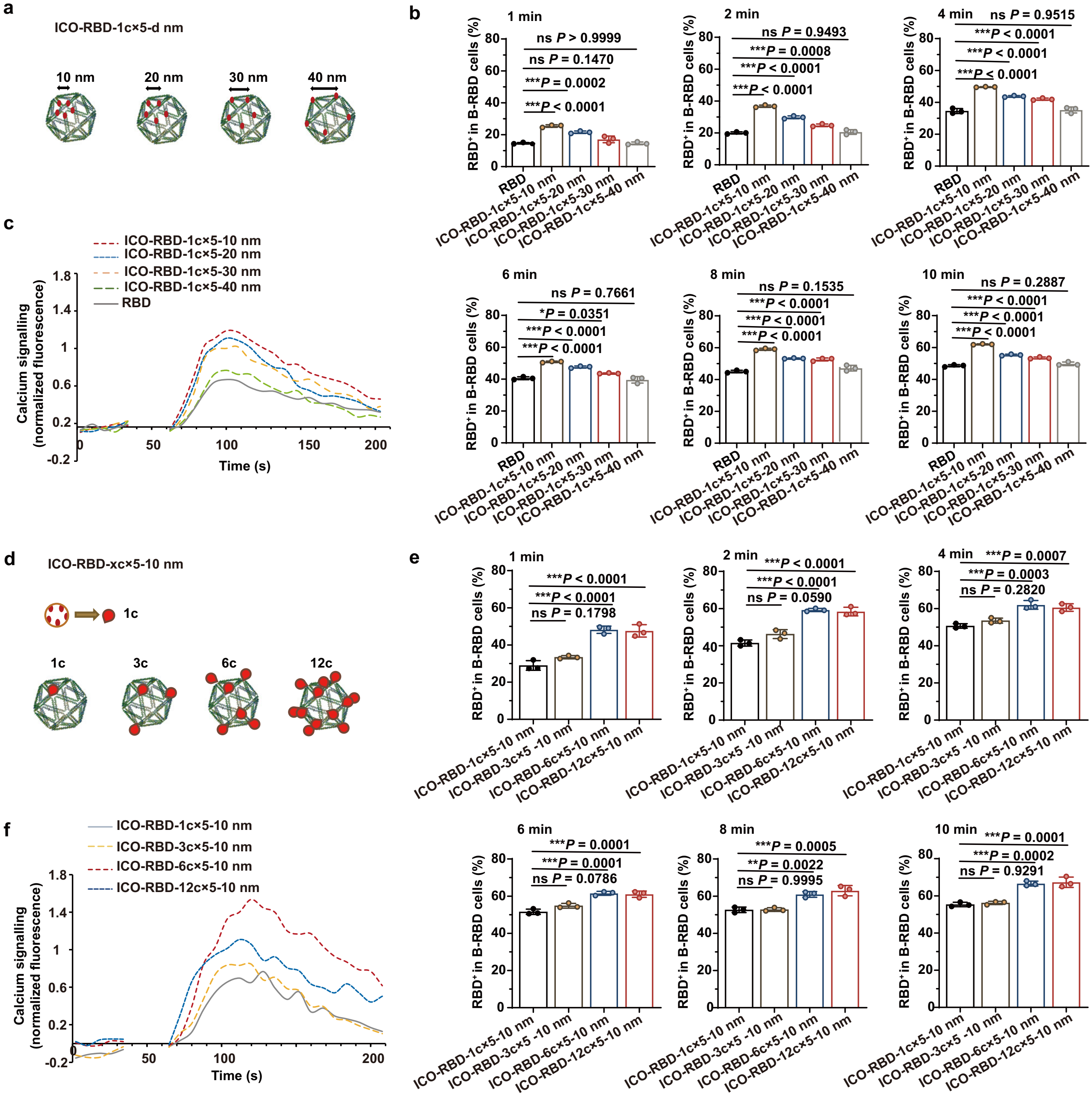

Fig. 2 | Effects of antigen spacing and cluster number on the efficiency of ICO-RBD nanovaccine activation of B-RBD cells. a Design of ICO-RBD nanovaccines with 1 RBD cluster of 5 RBD copies within clusters, but different RBD spacing from 10 to 40 nm. **b** Binding affinity between the SpyCatcher-RBD proteins (RBD) or ICO-RBD nanovaccines with different RBD spacing and B-RBD cells. ICO-RBD nanovaccines bound to B-RBD cells were detected using anti-His antibodies and flow cytometry ($n = 3$ independent experiments). **c** Ca^{2+} traces in B-RBD cells triggered by SpyCatcher-RBD proteins (RBD) or ICO-RBD nanovaccines with differing RBD spacing, as detected by Fluo-4 AM labeling and flow cytometry ($n = 3$ independent experiments). **d** Design of ICO-RBD nanovaccines with 1–12 RBD clusters of 5 RBD copies within clusters and 10 nm RBD spacing. **e** Binding affinity between the ICO-RBD nanovaccines with different RBD cluster numbers and B-RBD cells. ICO-RBD nanovaccines bound to B-RBD cells were detected using anti-His antibodies and flow cytometry ($n = 3$ independent experiments). **f** Ca^{2+} traces in B-RBD cells triggered by ICO-RBD nanovaccines with the different RBD cluster numbers, as detected by Fluo-4 AM labeling and flow cytometry measurement ($n = 3$ independent experiments). The data were processed on GraphPad Prism 8 and are presented as the mean ± SD. Statistical significance (P value) was calculated by one-way ANOVA followed by Tukey's test. $^{*}P < 0.05$; $^{**}P < 0.01$; $^{***}P < 0.001$. ns, $P > 0.05$, no significant difference. Source data are provided as a Source Data file.

elicited by ICO-RBD-6c × 5–10 nm were greater than 1×10^5, while the RBD monomers, RBD + ICO and other ICO-RBD nanovaccines, including ICO-RBD-1c × 5–10 nm, ICO-RBD-1c × 5–40 nm and ICO-RBD-6c × 1–10 nm, produced only 1×10^3–10^4 RBD-specific IgG titers (Fig. 3c). We monitored the RBD-specific IgG titers for 14 weeks; the time-titer curves in Fig. 3d show that the RBD-specific IgG titers in the ICO-RBD-6c × 5–10 nm group peaked at week 8 and only decreased slightly at week 14. However, the RBD-specific IgG titers in the other groups peaked at week 5 and decreased dramatically by week 14 (Fig. 3d). We used the sera collected at week 5 and 14 in pseudovirus neutralization testing to analyze the neutralizing antibodies, as represented by the inhibitory dilution value that achieved 50% neutralization (ID_{50}). Consistent with the RBD-specific IgG titer results, ICO-RBD-6c × 5–10 nm had ID_{50} values over 100 times greater than those in the RBD group (Fig. 3e, f). Further, the ICO-6C × 5–10 nm vaccine was compared with the ICO vaccine with a relatively uniform

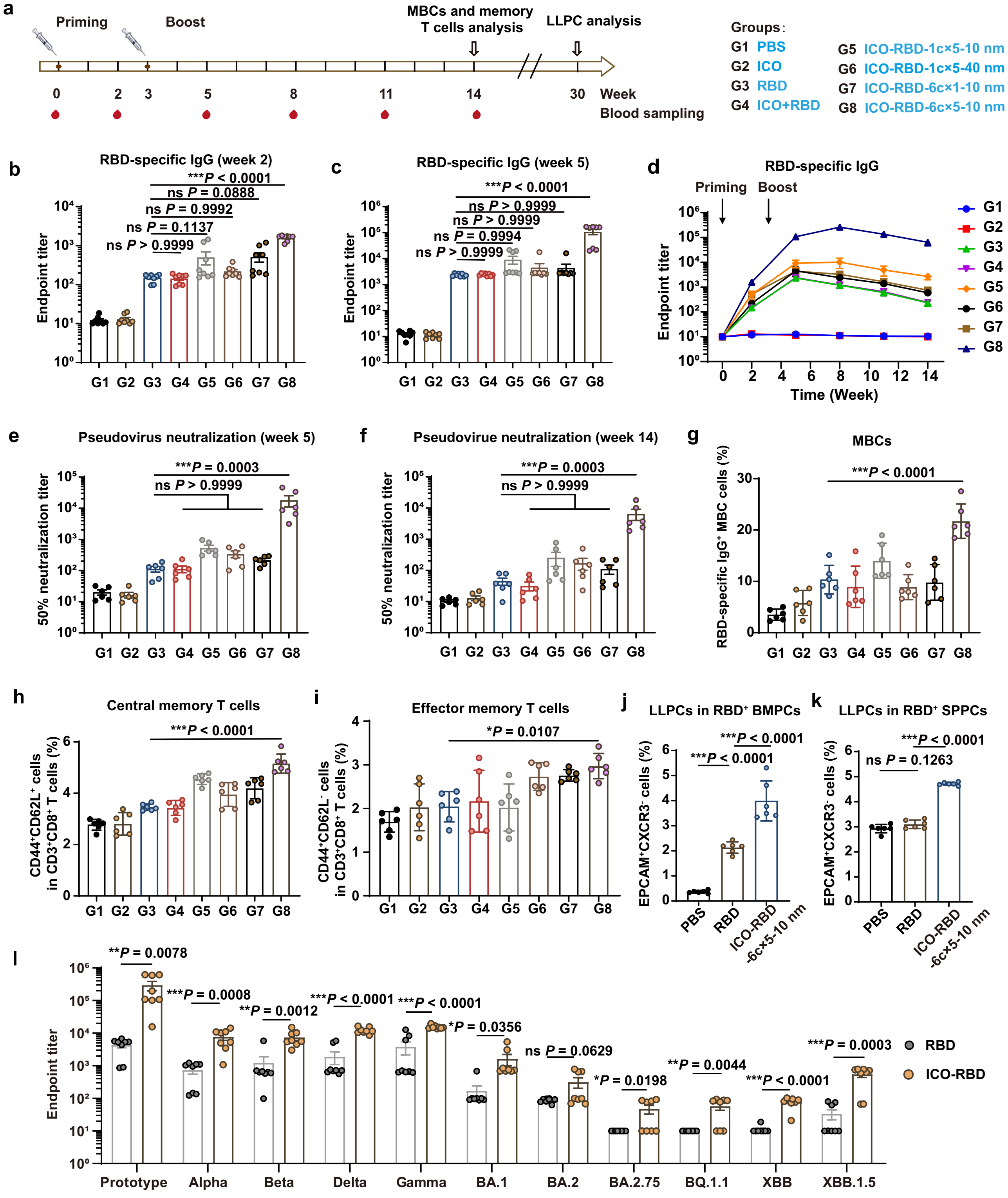

distribution of 30 RBDs, namely ICO (~43 nm)-RBD-UD and ICO (~90 nm)-RBD-UD vaccine. After the boost immunization, the RBD-specific IgG titers elicited by ICO-RBD-6c × 5–10 nm were greater than relatively uniform distributed RBD vaccines (Supplementary Fig. 6). Taken together, our data demonstrate that the ICO-RBD-6c × 5–10 nm nanovaccines were highly immunogenic compared to RBD monomers and relatively uniform distributed RBD nanovaccines.

Next, to assess whether the ICO-RBD nanovaccines can induce long-lasting immune effects, we evaluated the memory immune cells, including memory B cells (MBCs), effector memory T cells and central memory T cells at week 14, long-lived plasma cells (LLPCs) in week 30[39,40]. Compared with RBD monomers, the ICO-RBD-6c × 5–10 nm nanovaccines induced a significantly greater number of RBD-specific IgG$^+$ MBCs (Fig. 3g). Compared with mice in the RBD group, central memory T cells and effector memory T cells were significantly increased in the splenocytes from ICO-RBD-6c × 5–10 nm nanovaccine-immunized mice (Fig. 3h, i). The proportions of LLPCs in the RBD-specific bone marrow plasma cells and splenic plasma cells were also greater in the ICO-RBD-6c × 5-10 nm group than those in the RBD group (Fig. 3j, k and Supplementary Fig. 7a, b). In addition,

Fig. 3 | Humoral immune responses in ICO-RBD nanovaccine-immunized BALB/c mice. a Schematic illustration of the vaccination schedule and grouping information. The mice were randomly divided into 8 groups and were priming- and boost-vaccinated with the indicated vaccines containing prototype RBD at week 0 and 3, respectively. The red drop symbols indicate blood sampling and sera collection. SARS-CoV-2 RBD-specific IgG titers in serum, measured at week 2 (**b**) and 5 (**c**) by ELISA ($n = 8$ mice). Spycatcher-RBD proteins (prototype) were used to coat 96-well ELISA plates. **d** Time-titer curves of RBD-specific IgG titers measured every 3 weeks ($n = 8$ mice). **e, f** Pseudovirus neutralization test of the sera collected at week 5 and 14, as represented by the inhibitory dilution value to achieve 50% neutralization (ID_{50}; $n = 6$ mice). **g** Percentages of RBD^+ cells in IgG^+ MBCs ($B220^+CD38^+$) in splenocytes at week 14, as detected by flow cytometry ($n = 6$ mice). **h** Percentages of central memory T cells ($CD44^+CD62L^+$) in $CD3^+CD8^+$ T cells in splenocytes at week 14, as detected using flow cytometry ($n = 6$ mice). **i** Percentages of effector memory T cells ($CD44^+CD62L^-$) in $CD3^+CD8^+$ T cells in splenocytes at week 14, as detected using flow cytometry ($n = 6$ mice). **j, k** Percentages of LLPCs ($EpCAM^{hi}CXCR3^-$) in RBD^+ bone marrow plasma cells (BMPCs, $B220^-CD138^+$) and RBD^+ splenic plasma cells (SPPCs, $B220^-CD138^+$) at week 30, as detected using flow cytometry ($n = 6$ mice). **l** Serum titers of IgG against variants, measured at week 5 by ELISA ($n = 8$ mice). Different RBD proteins were used to coat 96-well ELISA plates, including prototype (Wuhan-Hu-1 strain), Alpha [B.1.1.7], Beta [B.1.351], Gamma [P.1], Delta [B.1.617.2] and Omicron [BA.1, BA.2, BA.2.75, BQ.1.1, XBB and XBB.1.5]. The data are presented as the mean ± SEM in panels **b**–**f** and **l**, and the mean ± SD in panels **g**–**k**. The data were processed on GraphPad Prism 8. Statistical significance (P value) was calculated by one-way ANOVA followed by Tukey's test in panels **b**, **c** and **e**–**k**, a two-tailed unpaired t test in panel l. $^{**}P < 0.01$; $^{***}P < 0.001$. ns, $P > 0.05$, no significant difference. Source data are provided as a Source Data file.

Interestingly, the numbers of these memory immune cells were highest in the ICO-RBD-6c × 5-10 nm group, as compared to those in other ICO-RBD nanovaccine groups with different surface RBD patterns. These results indicate that the relationship between surface antigen pattern and nanovaccine efficiency still works in vivo.

Finally, to assess the broad spectrum of RBD monomers and ICO-RBD-6c × 5–10 nm nanovaccines containing prototype RBD, we used a panel of SARS-CoV-2 RBD antigens to test the serum titers of IgG against the protype and the variants, including prototype (Wuhan-Hu-1 strain), Alpha [B.1.1.7], Beta [B.1.351], Gamma [P.1], Delta [B.1.617.2] and Omicron [BA.1, BA.2, BA.2.75, BQ.1.1, XBB and XBB.1.5]. As shown in Fig. 3i, the ICO-RBD-6c × 5–10 nm nanovaccines induced more IgG against all variants than the RBD monomers. In particular, for Omicron [BA.1], [BA.2] and [XBB.1.5], the IgG titers in the ICO-RBD-6c × 5–10 nm nanovaccine group reach to 1608, 315 and 544, respectively, being significantly higher than 168, 86 and 33 in the RBD group (Fig. 3i). This is an interesting phenomenon, since the immune escape against Omicron variants is a widespread problem in the prototype RBD vaccines. By optimized assembly on the DNA origami scaffold, the ICO-RBD nanovaccines (prototype) can activate an observable antibody response against Omicron variants, which is important for the prevention of SARS-CoV-2 as the variants continue to emerge. These results are similar to a recent study in which the multivalent antigen display on nanoparticles of respiratory syncytial virus increased the B cell clonotype diversity and neutralization breadth[41]. Moreover, the ICO-RBD vaccine did not exhibit any cross-reactivity with varicella-zoster virus antigen (glycoprotein E, gE) and influenza virus antigens (haemagglutinin protein, HA protein) (Supplementary Fig. 8), indicating that ICO-RBD vaccine has excellent antigen specificity.

To further investigate the protection ability of ICO-RBD nanovaccines against SARS-CoV-2, 7-week-old female Syrian hamsters were immunized with RBD monomer and ICO-RBD vaccines, respectively. These hamsters were intranasally challenged with 10^4 TCID50 authentic SARS-CoV-2 viral particles (WH-01 strain) at two weeks post boost vaccination, and viral RNA of nasal washes and lungs were analyzed (Supplementary Fig. 9a). At day 4 and 6 after infection, the viral load of nasal washes in the ICO-RBD group was 54.7% and 96.7% lower than those in the RBD monomer group, respectively (Supplementary Fig. 9b). Viral load analysis of lung tissue showed that ICO-RBD vaccine group was also significantly lower than that of RBD monomer vaccine group (Supplementary Fig. 9c). These data support that ICO-RBD nanovaccines reduced the SARS-CoV-2 infection.

In summary, the DNA origami-based nanovaccines induced markedly increased neutralization antibodies against RBD and 1.5-fold more RBD-specific memory immune cells than RBD monomers, which is expected to provide a persistent protective humoral response. In addition, the ICO-RBD vaccine effectively reduced authentic viral load in nasal and lung tissue.

In vivo induction of T cell immune responses by ICO-RBD nanovaccines

There are numerous $CD4^+$ and $CD8^+$ T cell epitopes in the RBD proteins, which are also critical for virus defense and clearance[42,43]. Next, to measure the T cell responses induced by the ICO-RBD nanovaccines (ICO-RBD-6c × 5–10 nm), we performed intracellular cytokine staining assays to analyze the different T cell populations within the spleen and lung at week 3 and 6, respectively. As shown in Fig. 4a–d, the ICO-RBD nanovaccines elicited more RBD-specific $CD8^+$ and $CD4^+$ T cells expressing interferon-γ (IFN-γ), interleukin (IL)-2 and tumor necrosis factor-α (TNF-α) than RBD monomers, in both spleen and lung tissue, indicating that ICO-RBD nanovaccines induced strong type 1 T helper cell (Th1)-biased immune responses in vivo. IL-4 expressing $CD4^+$ T cells were rarely induced across the three groups after priming and boost immunization, indicating that Th2-biased immune cells were not evoked (Fig. 4e, f). Tissue resident memory T cells (TRMs) rapidly mobilize innate and adaptive immunity to achieve antiviral status in the lung[44]. As shown in Fig. 4g, RBD monomers did not induce apparent TRMs in the lung tissues, however the ICO-RBD nanovaccines generated 1.5-fold more TRMs in the lungs after boost immunization. Together, these results indicate that the ICO-RBD nanovaccines were able to induce marked T cell immune responses in addition to the B cell responses.

ICO-RBD nanovaccine induction of antigen presentation and germinal center responses in drainage lymph nodes

To further elucidate how ICO-RBD nanovaccines are recognized and processed by the host immune system, and participate in immune responses, we intramuscularly injected mice with Cy5.5-labeled RBD monomers or ICO-RBD nanovaccines (ICO-RBD-6c × 5–10 nm) and isolated the inguinal lymph nodes after different time intervals (up to 14 days). As shown in Fig. 5a, compared with RBD monomers, an increased amount of the ICO-RBD nanovaccines accumulated in the inguinal lymph nodes. A fraction of ICO-RBD nanovaccines was still present in the inguinal lymph nodes until day 7 (Fig. 5a), which facilitated long-term immune stimulation of B and T cells.

Immunofluorescence detection of inguinal lymph nodes showed that the ICO-RBD nanovaccines and dendritic cells (DCs) were obviously co-localized on day 1, 3 and 5 after the priming immunization in the ICO-RBD group (Fig. 5b). A detailed analysis of vaccine uptake by antigen-presenting cells indicated that DCs ($CD11C^+$), mature DCs ($CD11C^+CD80^+$ and $CD11C^+CD86^+$) and macrophages ($F4/80^+$) captured 1.6, 1.8, 1.9 and 2.2 times, respectively, amount of ICO-RBD nanovaccines compared to RBD monomers (Supplementary Fig. 10a–d). There were no significant differences in the amounts of ICO-RBD nanovaccines or RBD monomers captured by $CD103^+$ migrated DCs ($CD11C^+CD103^+$) (Supplementary Fig. 10e). However, differences were evident in the $CD103^-$ resident DCs ($CD11C^+CD103^-$), as well as in the follicular DCs ($CD11C^+CD21/CD35^+$; Supplementary Fig. 10f, g). Long-term monitoring of follicular DCs showed that ICO-RBD nanovaccines

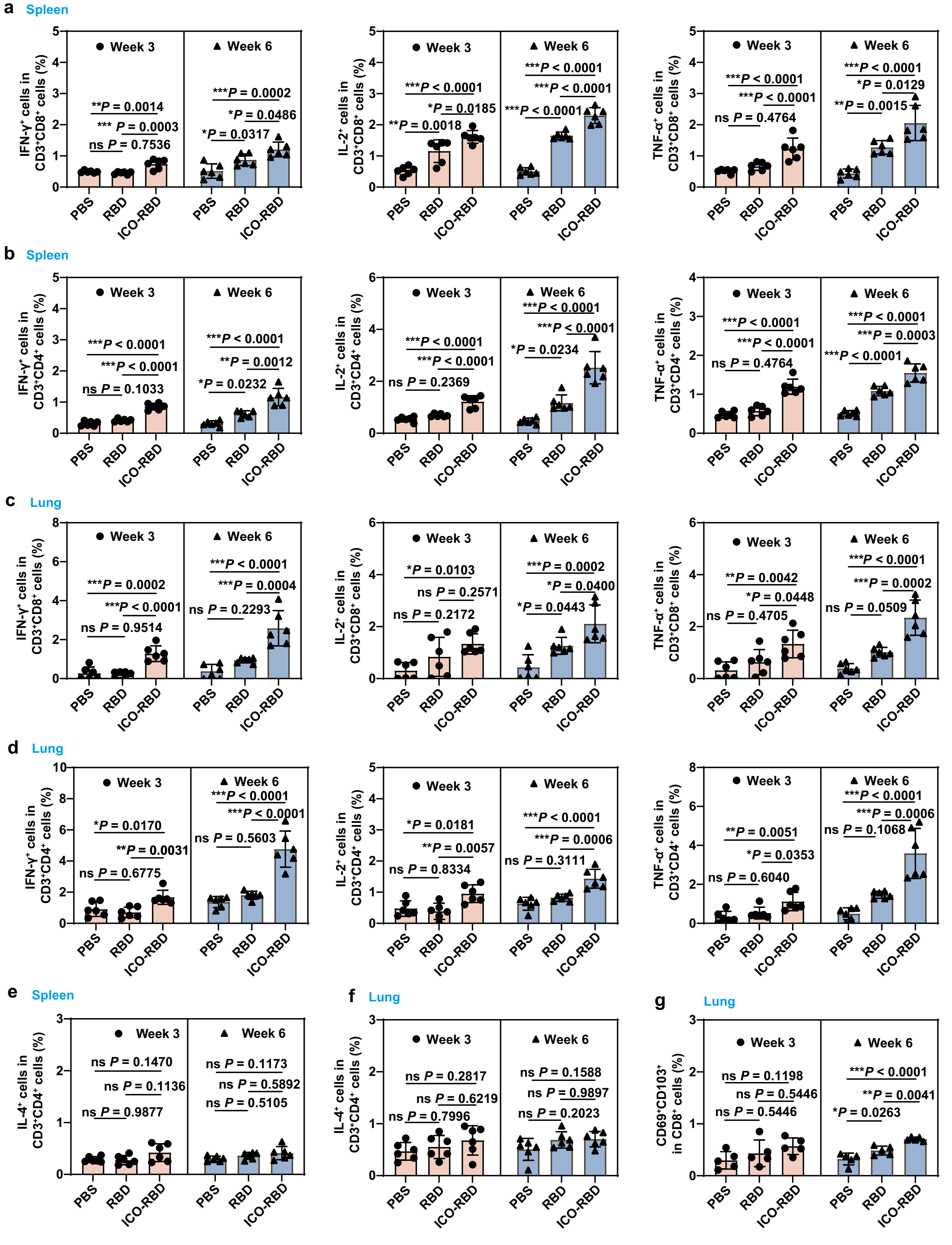

existed in follicular DCs for a longer time than RBD monomers (Fig. 5c), which was conducive for follicular DCs to display the antigens on the surface and present them to B cells[45]. Thus, the ICO-RBD nanovaccines actively drained into the lymph nodes after intramuscular injection, and were more easily captured by resident and follicular DCs than monomeric RBD, which may contribute to the enhanced B and T cell immunity induced by the ICO-RBD nanovaccines.

Nanoparticle vaccines are more easily captured by DCs and macrophages than soluble vaccines, thus promoting the coordination of T follicular helper cells (T_{FH}) and B cells, which is required for a prolonged and effective vaccination to drive antibody-mediated humoral immunity[36,46]. To evaluate the germinal center responses, we measured T_{FH} cells ($CD4^+PD1^+CXCR5^+$), germinal center (GC) B cells ($CD19^+B220^+GL7^+CD95^+$) and plasma cells ($CD44^+CD138^+$) in the

Fig. 4 | T cell responses induced by ICO-RBD nanovaccines in mice. The mice were randomly divided into 3 groups and priming- and boost-vaccinated with the indicated vaccines at week 0 and 3, respectively. The spleens and lungs of mice were harvested at week 3 (before boost immunization) and 6. The harvested cells were stimulated with SpyCatcher-RBD proteins overnight. Proportions of IFN-γ$^+$/IL-2$^+$/TNF-α$^+$ cells in CD3$^+$CD8$^+$ T cells (**a**) and CD3$^+$CD4$^+$ T cells (**b**) within the spleen, as detected using intracellular cytokine staining assays and flow cytometry ($n = 6$ mice). Proportions of IFN-γ$^+$/IL-2$^+$/TNF-α$^+$ cells in CD3$^+$CD8$^+$ T cells (**c**) and CD3$^+$CD4$^+$ T cells (**d**) within the lung, as detected using intracellular cytokine staining assays and flow cytometry ($n = 6$ mice). Proportions of IL-4$^+$ cells in CD3$^+$CD4$^+$ T cells within the spleen (**e**) and lung (**f**), as detected using intracellular cytokine staining assays and flow cytometry ($n = 6$ mice). **g** Percentages of CD69$^+$CD103$^+$ TRMs in CD8$^+$ T cells in the lung, as detected using flow cytometry ($n = 5$ mice). The data were processed on GraphPad Prism 8 and are presented as the mean ± SD. Statistical significance (P value) was calculated by one-way ANOVA followed by Tukey's test. $^*P < 0.05$; $^{**}P < 0.01$; $^{***}P < 0.001$. ns, $P > 0.05$, no significant difference. Source data are provided as a Source Data file.

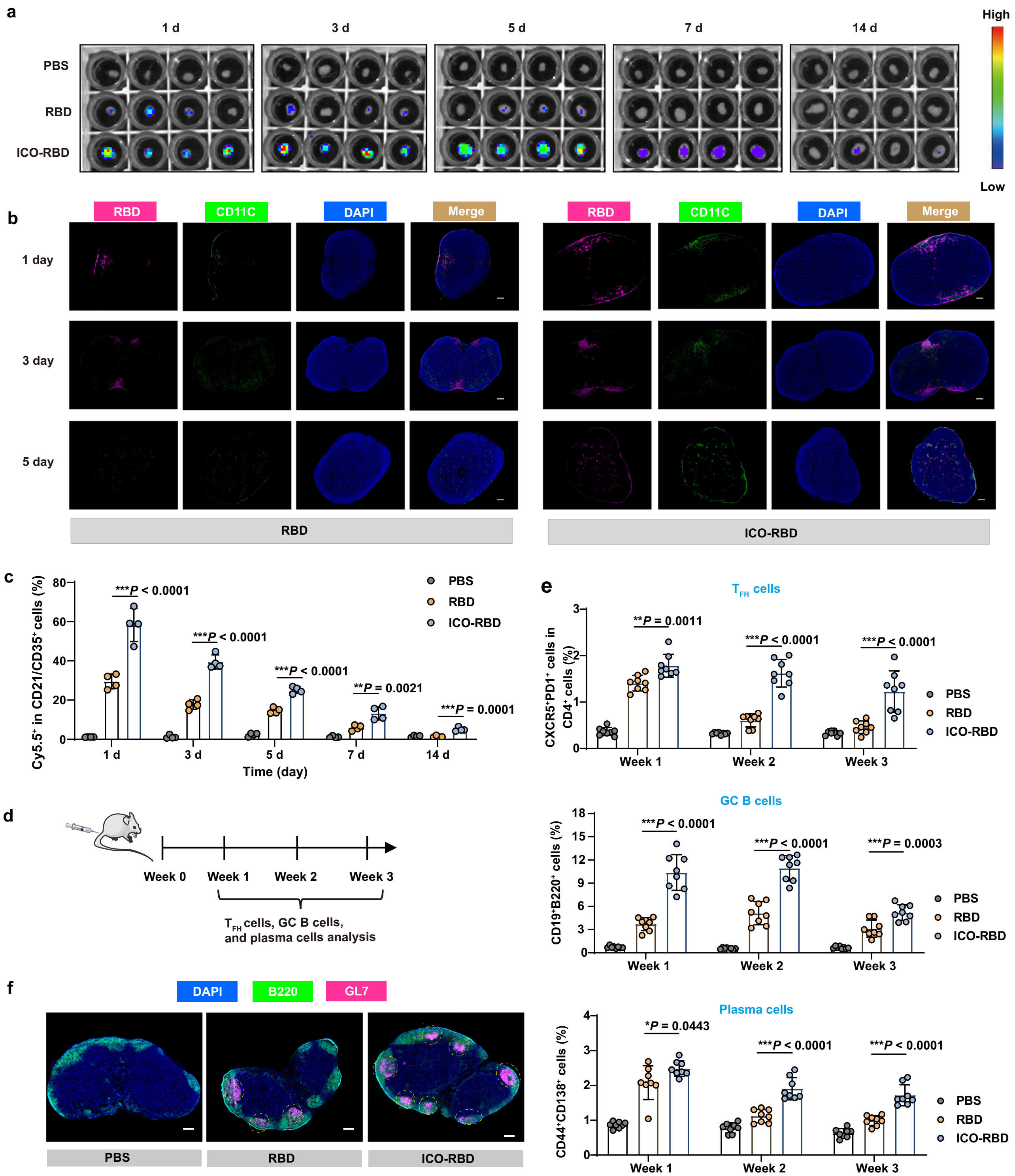

Fig. 5 | Antigen presentation and germinal center responses in drainage lymph nodes induced by ICO-RBD nanovaccines. a ICO-RBD nanovaccine accumulation in lymph nodes. BALB/c mice were intramuscularly immunized with Cy5.5-labelled RBD monomers (SpyCatcher-RBD proteins) or Cy5.5-labelled ICO-RBD nanovaccines. After different time intervals, the inguinal lymph nodes were obtained and then fluorescence imaging was performed (*n* = 4 mice).**b** Immunofluorescence detection of inguinal lymph nodes on day 1, 3 and 5. Green, CD11C$^+$ DCs; Red, Cy5.5-labelled RBD. Scale bar, 200 μm. **c** Percentages of CD21/CD35$^+$Cy5.5$^+$ follicular DCs in CD11C$^+$ DCs in the inguinal lymph nodes after different time up to 14 days, as detected using flow cytometry (*n* = 4 mice). **d** Schematic illustration of the experiment schedule to analyze germinal center responses. BALB/c mice were randomly divided into PBS, RBD and ICO-RBD groups. The inguinal lymph nodes were harvested at week 1, 2 and 3 after priming immunization. **e** Percentages of T$_{FH}$ cells (CXCR5$^+$PD1$^+$) in CD4$^+$ cells, GC B cells (CD95$^+$GL7$^+$) in CD19$^+$B220$^+$ cells and plasma cells (CD44$^+$CD138$^+$), as detected using flow cytometry (*n* = 8 mice).**f** Immunofluorescence detection of inguinal lymph nodes on week 5. The mice were intramuscularly immunized with two doses of 50 μL nanovaccines containing 1 μg SpyCatcher-RBD at week 0 and 3, mixed with 50 μL AddaVax. The white circles indicate the germinal centers, in which there are B220$^+$GL7$^+$ GC B cells. Scale bar, 200 μm. These experiments (**b**, **f**) were repeated three times independently with similar results. The data were processed on GraphPad Prism 8 and are presented as the mean ± SD. Statistical significance (*P* value) was calculated by one-way ANOVA followed by Tukey's test. $^*P < 0.05$; $^{**}P < 0.01$; $^{***}P < 0.001$. Source data are provided as a Source Data file.

inguinal lymph nodes at week 1, 2 and 3 after the priming immunization (Fig. 5d). Although RBD monomers evoked measurable T$_{FH}$ cell, GC B cell and plasma cell responses, induction with the ICO-RBD nanovaccines elicited respective responses in these cell populations that were 2.7, 2.1 and 1.7 times greater at week 2 (Fig. 5e). Importantly, the ICO-RBD nanovaccines maintained elevated frequencies of T$_{FH}$ cells, GC B cells and plasma cells for a longer period than RBD monomers, as indicated by the 2.7-, 1.7- and 1.7-fold greater responses of these cells at week 3 (Fig. 5e). The serum titers of RBD-specific IgG in the ICO-RBD nanovaccine group gradually increased from week 1 to week 3, while the serum titers in the RBD group remained stable (Supplementary Fig. 11a, b). On week 5, there were more germinal centers in the inguinal lymph nodes in the ICO-RBD nanovaccine group than those in the RBD group (Fig. 5f). Taken together, our data demonstrate that the ICO-RBD nanovaccines were more effectively captured by antigen-presenting cells and stimulated stronger germinal center responses than RBD monomers, thus enabling more effective antigen presentation, T-B crosstalk and B cell maturation.

Comparison of ICO-RBD nanovaccines and trimeric mRNA vaccines containing Omicron RBD

To verify the compatibility of ICO scaffold for different antigens, we constructed ICO-RBD-6c × 5–10 nm nanovaccines containing Omicron RBD (ICO-RBD$_{omic}$). We used the similar "engraving-printing" strategy to decorate the RBD proteins of Omicron [B.1.1.529] onto ICO, except that the part responsible for the connection of RBD to polyT changed from SpyCatcher-SpyTag ligation to His-Nitrilotriacetic acid (NTA) affinity. For trimeric mRNA vaccines containing Omicron RBD (mRNA-RBD$_{omic}$), we transcribed the RBD mRNA of Omicron [B.1.1.529] containing the C-terminal T4 fibritin foldon trimerization domain in vitro, and adopted the same lipid nanoparticle formulation as that of BNT162b2 to deliver mRNA and prepare mRNA-RBD$_{omic}$[47].

Mice were immunized with two intramuscular injections of RBD$_{omic}$, mRNA-RBD$_{omic}$ and ICO-RBD$_{omic}$, respectively, formulated with AddaVax adjuvant (Fig. 6a). Both mRNA-RBD$_{omic}$ vaccines and ICO-RBD$_{omic}$ nanovaccines stimulated similar levels of RBD$_{omic}$-specific IgG titers, both being dramatically higher than those in the RBD$_{omic}$ group, either at week 2 after priming immunization or at week 5 after boost immunization (Fig. 6b, c). In terms of broad spectrum, the IgG in both mRNA-RBD$_{omic}$ and ICO-RBD$_{omic}$ groups were able to recognize RBD of all 11 variants we examined (Fig. 6d, e). However, the ICO-RBD$_{omic}$ nanovaccines activated more IL-2$^+$CD4$^+$ and TNF-α$^+$CD8$^+$ T cells than the mRNA-RBD$_{omic}$ vaccines (Fig. 6f and Supplementary Fig. 12a–c). In addition, there was no apparent TRMs in the lung tissues in the mRNA-RBD$_{omic}$ group, and the ICO-RBD$_{omic}$ nanovaccines generated 3.3-fold more TRMs in the lungs after boost immunization (Fig. 6g). In general, compared with the trimeric mRNA vaccines, the ICO-RBD nanovaccines stimulated similar humoral immune effects and exhibited an observable advantage in T cell immune activation.

Next, we evaluated the RBD$_{omic}$-specific IgG titers, memory immune cells, including MBCs, LLPCs, effector memory T cells and central memory T cells, at week 14. Interestingly, the mRNA-RBD$_{omic}$ vaccines and ICO-RBD$_{omic}$ nanovaccines kept similar levels of IgG titers at week 14 (Fig. 6h). We evaluated the germinal center responses in the inguinal lymph nodes and found that the ICO-RBD$_{omic}$ nanovaccines maintained elevated frequencies of T$_{FH}$ cells, and B cells for a longer period than mRNA-RBD$_{omic}$ vaccines at week 14 (Supplementary Fig. 13a–d). In addition, the ICO-RBD^{omic} nanovaccines activated more TNF-α$^+$CD4$^+$ and TNF-α$^+$CD8$^+$ T cells than the mRNA-RBD$_{omic}$ vaccines (Supplementary Fig. 14a, c). Compared with the mRNA-RBD$_{omic}$ vaccines, the ICO-RBD$_{omic}$ nanovaccines induced a significantly greater number of RBD-specific IgG$^+$ MBCs (Fig. 6i). The proportions of LLPCs in the RBD-specific bone marrow plasma cells and splenic plasma cells were also greater in the ICO-RBD$_{omic}$ group than those in the mRNA-RBD$_{omic}$ group (Fig. 6j, k and Supplementary Fig. 15a, b). In addition, although the mRNA-RBD$_{omic}$ vaccines generated more central memory T cells (Supplementary Fig. 15c), the mRNA-RBD$_{omic}$ vaccines and ICO-RBD$_{omic}$ nanovaccines induced similar levels of effector memory T cells, both being higher than those in the RBD$_{omic}$ group (Fig. 6l).

Compared to subunit protein vaccines, the nucleic acid-based vaccines mimics infection or immunization with live microorganisms. Therefore, the nucleic acid-based vaccines can generate cell-mediated immunity at the same time as humoral immunity, and the subunit protein vaccines require adjuvants to activate effective cell-mediated immunity. However, our ICO-displayed subunit nanovaccines activated robust cell-mediated immunity, even higher than the mRNA vaccines. Considering that ICO was derived from the assembly of genomic DNA of M13mp18 bacteriophage, ICO not only has the function as a scaffold to display subunit antigens, but also may have the function as an adjuvant similar to nucleic acid-based vaccines to mimics viral invasion, which is a potential advantage of the DNA-based nanocarriers.

Immunogenicity of ICO scaffold and biosafety of ICO-RBD nanovaccines

To analyze the immunogenicity of ICO scaffold in vitro and in vivo, bone marrow-derived dendritic cells (BMDCs) were isolated and treated with different concentrations of ICO. As shown in Fig. 7a, ICO can stimulate BMDCs' maturation in a dose-dependent manner, indicated by the gradual increase of CD80$^+$CD86$^+$ BMDCs. Even after decoration of RBD, ICO-RBD still possessed the ability to stimulate BMDCs' maturation (Fig. 7a). After intramuscular injection, ICO also generated an obvious elevation of CD80$^+$CD86$^+$ DCs in the drainage lymph nodes (Fig. 7b). These results suggest that ICO are inherently immunogenic.

Subsequently, we assessed whether the immunogenicity of ICO scaffold could replace adjuvants in the vaccination. Mice received two intramuscular injections of ICO-RBD nanovaccines and ICO-RBD nanovaccines without AddaVax adjuvant (ICO-RBD without AddaVax), respectively (Fig. 7c). Although the RBD-specific IgG titers in the ICO-RBD and ICO-RBD without AddaVax groups were similar after priming immunization, the IgG titers in the ICO-RBD group were significantly higher than those in the ICO-RBD without AddaVax group after boost immunization (Fig. 7d). Therefore, the additional adjuvant is still necessary for our ICO-based nanovaccines.

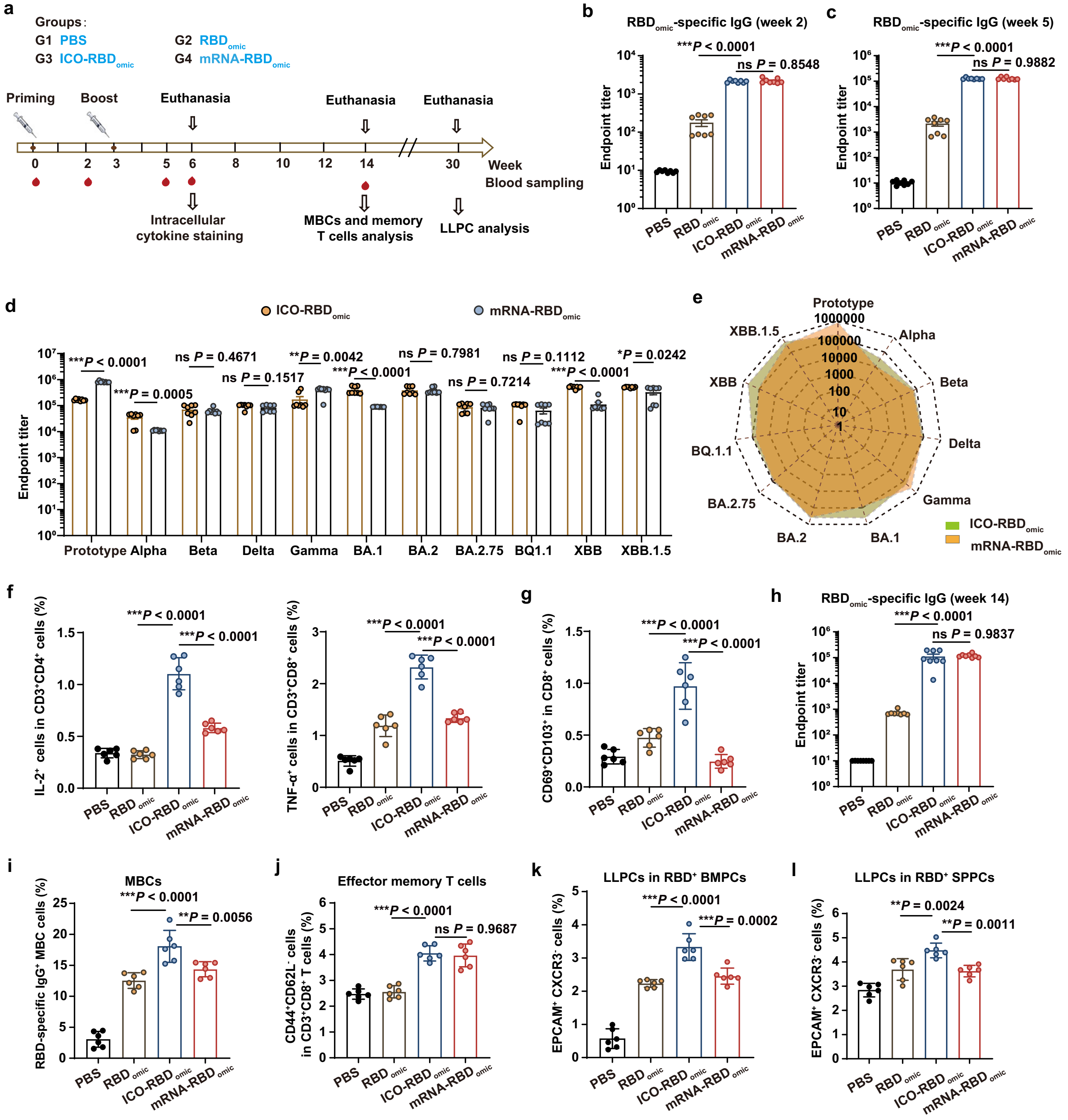

Fig. 6 | Comparison of ICO-RBD nanovaccines and trimeric mRNA vaccines containing Omicron RBD. **a** Schematic illustration of the vaccination schedule. Omicron RBD-specific IgG titers in serum, measured at week 2 (**b**) and 5 (**c**) by ELISA ($n = 8$ mice). **d** Serum titers of IgG against variants, measured at week 5 by ELISA ($n = 8$ mice). Different RBD proteins were used to coat 96-well ELISA plates, including prototype (Wuhan-Hu-1 strain), Alpha [B.1.1.7], Beta [B.1.351], Gamma [P.1], Delta [B.1.617.2] and Omicron [BA.1, BA.2, BA.2.75, BQ.1.1, XBB and XBB.1.5]. **e** Radar plot demonstrating IgG serum titers of the ICO-RBD$_{omic}$ and mRNA-RBD$_{omic}$ vaccines against 11 RBD variants. **f** Proportions of IL-2$^+$ cells in CD3$^+$CD4$^+$ T cells and TNF-α$^+$ cells in CD3$^+$CD8$^+$ T within the spleen, as detected at week 6 using intracellular cytokine staining assays and flow cytometry ($n = 6$ mice). **g** Percentages of CD69$^+$CD103$^+$ TRMs in CD8$^+$ T cells in the lung, as detected at week 6 using flow cytometry ($n = 6$ mice). **h** Omicron RBD-specific IgG titers in serum, measured at week 14 by ELISA ($n = 8$ mice). **i** Percentages of RBD$^+$ cells in IgG$^+$ MBCs (B220$^+$CD38$^+$) in splenocytes at week 14, as detected by flow cytometry ($n = 6$ mice). Percentages of LLPCs (EpCAM^{hi}CXCR3$^-$) in RBD$^+$ bone marrow plasma cells (BMPCs, B220$^-$CD138$^+$) (**j**) and RBD$^+$ splenic plasma cells (SPPCs, B220$^-$CD138$^+$) (**k**) at week 30, as detected using flow cytometry ($n = 6$ mice). **l** Percentages of effector memory T cells (CD44$^+$CD62L$^-$) in CD3$^+$CD8$^+$ T cells in splenocytes at week 14, as detected using flow cytometry ($n = 6$ mice). The data were processed on GraphPad Prism 8. The data are presented as the mean ± SEM in panel **b**–**d** and **h**, and the mean ± SD in panels **f**, **g** and **i**–**l**. Statistical significance (P value) was calculated by one-way ANOVA followed by Tukey's test in panels **b**, **c** and **f**–**l**, and a two-tailed unpaired t test in panel **d**. $^*P < 0.05$; $^{**}P < 0.01$; $^{***}P < 0.001$. ns, $P > 0.05$, no significant difference. Source data are provided as a Source Data file.

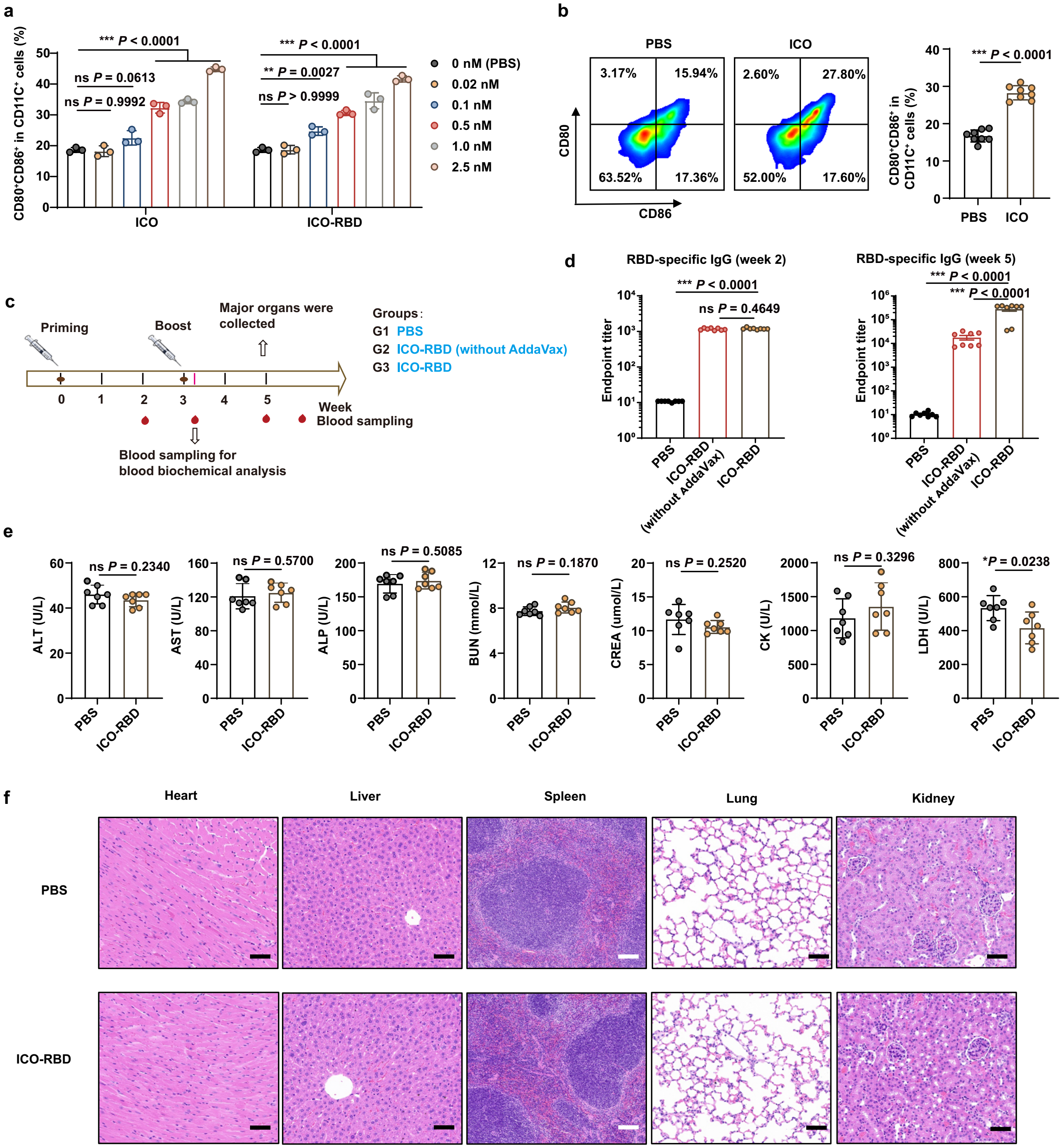

Fig. 7 | Immunogenicity of ICO scaffold and biosafety of ICO-RBD nanovaccines. **a** Percentages of CD80⁺CD86⁺ in CD11C⁺ cells in BMDCs after treatment with different concentrations of ICO for 12 h, as detected using flow cytometry ($n = 3$ independent experiments). **b** Percentages of CD80⁺CD86⁺ in CD11C⁺ DCs in the inguinal lymph nodes, as detected using flow cytometry ($n = 8$ mice). Mice were intramuscularly injected with two doses of ICO at week 0 and 3, and the inguinal lymph nodes were harvested after 3 weeks. **c** Schematic illustration of the vaccination schedule. Mice were randomly divided into 3 groups: PBS (control), ICO-RBD nanovaccines without AddaVax (ICO-RBD without AddaVax), and ICO-RBD nanovaccines with AddaVax (ICO-RBD vaccines). Mice were intramuscularly immunized with two doses of ICO-RBD nanovaccines at week 0 and 3, mixed with or without 50 μL AddaVax. **d** RBD-specific IgG titers in serum, measured at week 2 and 5 by ELISA ($n = 8$ mice). Blood biochemical analysis (**e**, $n = 7$ mice) at day 22 and histological evaluation of major organs (**f**) at week 5. These experiments (**f**) were repeated three times independently with similar results. Black scale bar, 50 μm, white scale bar, 100 μm. Mice were intramuscularly immunized with two doses of ICO-RBD nanovaccines at week 0 and 3, mixed with 50 μL AddaVax. The data were processed on GraphPad Prism 8. The data are presented as the mean ± SEM in panel **d**, and the mean ± SD in panel **a**, **b** and **e**. Statistical significance (P value) was calculated by one-way ANOVA followed by Tukey's test in panels a and d, and a two-tailed unpaired t test in panels **b** and **e**. $^{*}P < 0.05$; $^{***}P < 0.001$. ns, $P > 0.05$, no significant difference. Source data are provided as a Source Data file.

Finally, we evaluated the biosafety of ICO-RBD nanovaccines. Two intramuscular injections of ICO-RBD nanovaccines did not induce significant changes in blood biochemical analysis (Fig. 7e), nor did they cause obvious histological abnormalities in major organs (Fig. 7f).

In summary, we employed an icosahedral DNA origami, ICO, to construct tailor-made nanovaccines with shapes and sizes closely resembling SARS-CoV-2, as an RBD antigen display platform. Based on an "engraving-printing" strategy that can efficiently and specifically link site-modified RBD antigens onto the surface of ICO, we achieved a rational design and accurate assembly of SARS-CoV-2 RBD nanovaccines. We also scrutinized several parameters of the surface antigen pattern, including antigen spacing, antigen copies within clusters and cluster numbers, for their influence on B cell activation. Finally, we systematically evaluated the immunogenicity of the optimized nanovaccines, ICO-RBD-6c × 5-10 nm, which evoked more robust and enduring humoral and T cell immune responses than soluble RBD antigens in mice, and the multivalent display broadened the protection range of B cell responses to more mutant strains. The ICO scaffold and the optimized surface antigen pattern were also suitable for the display of Omicron RBD, and the constructed nanovaccines exhibited the comparable immune effects in humoral immunity as the mRNA vaccines and a stronger ability to activate cellular immunity. The structure-function relationship between antigen configuration and immunogenicity that we demonstrate through the use of the DNA origami platform may pave the way for the future development of potent vaccines for SARS-CoV-2 and/or other viruses.

Methods

Reagents and materials

Oligonucleotides, purified by polyacrylamide gel electrophoresis (PAGE), used for folding ICO were synthesized by Beijing Ruibio Biotech Co., Ltd (Beijing, China). The genomic DNA of M13mp18 bacteriophage was obtained from Beijing Intell Nanomedicine (Beijing, China). DBCO-polyT (20 × T), SpyTag-N3, Cy5.5-SpyTag and FITC-SpyTag were synthesized by China Peptides Co., Ltd. (Shanghai, China). The RBD-specific BCR expression plasmid, pRRL EuB29 COVA2-15 IgGTM. BCR. GFP. WPRE was a kind gift from Drs. Marit J. van Gils and Rogier W. Sanders in the Department of Medical Microbiology at the University of Amsterdam. The SARS-CoV-2 pseudovirus neutralization test kit (Cat: #L02087A), including the SARS-CoV-2 pseudovirus Luc Reporter and HEK-293 cells expressing hACE2, was purchased from GenScript (Nanjing, China).

The antibodies used for flow cytometry were as follows: anti-His Tag APC (BioLegend, USA, Cat: #362605), anti-human IgG (G18-145) APC (BD, USA, Cat: #550931), anti-mouse CD3 APC (BioLegend, Cat: #100312), anti-mouse CD19 APC (BioLegend, Cat: #115512), anti-mouse CD138 APC (Biolegend, Cat: #142506), anti-mouse CXCR5 APC (Biolegend, Cat: #145506), anti-mouse CD103 APC (Biolegend, Cat: #121414), anti-mouse CD8 FITC (Biolegend, Cat: #100706), anti-mouse CD11C FITC (Biolegend, Cat: #117306), anti-mouse CD95 (Fas) FITC (Biolegend, Cat: #152606), anti-mouse IgG FITC (Biolegend, Cat: #406001), anti-mouse CD4 PE (Invitrogen, USA, Cat: #12-0042-85), anti-mouse CD44 PE (Biolegend, Cat: #103008), anti-mouse CD80 PE (Biolegend, Cat: #104708), anti-mouse CXCR3 PE (Biolegend, Cat: #126505), anti-mouse CD103 PE (Biolegend, Cat: #121406), anti-mouse CD21/CD35 PE (Biolegend, Cat: #123410), anti-mouse CD69 PE (Biolegend, Cat: #104508), anti-mouse CD86 PE/Cyanine7 (Biolegend, Cat: #105014), anti-mouse IFNγ PE/Cyanine7 (Biolegend, Cat: #505826), anti-mouse F4/80 PE/Cyanine7 (Biolegend, Cat: #123114), anti-mouse CD279 (PD-1) PE/Cyanine7 (Biolegend, Cat: #109109), anti-mouse/human GL7 PE/Cyanine7 (Biolegend, Cat: #144619), anti-mouse EpCAM PE/Cyanine7 (Biolegend, Cat: #118215), anti-mouse CD38 PE/Cyanine7 (Biolegend, Cat: #102718), anti-mouse IL2 PE/Cyanine7 (Biolegend, Cat: #503831), anti-mouse IL4 PE/Cyanine7 (Biolegend, Cat: #504117), anti-mouse TNF-α PE/Cyanine7 (Biolegend, Cat: #506323), anti-mouse CD62L PE/Cyanine7 (Biolegend, Cat: #104418), anti-mouse CD8a PE/Cyanine7 (Biolegend, Cat: #100722), anti-mouse/human B220 APC/Cyanine7 (Biolegend, Cat: #103223), anti-mouse CD4 PerCP (Biolegend, Cat: #100432).

The antibodies used for immunofluorescent staining were as follows: Alexa Fluor™ 488 conjugated CD11C (N418) antibody (eBioscience, USA, Cat: 53-0114-82), anti-mouse Alexa Fluor™ 488 conjugated B220 (RA3-6B2) antibody (eBioscience, Cat: 53-0452-82), Alexa Fluor® 647 anti-mouse/human GL7 antigen (Biolegend, Cat:144605).

Protein expression and purification

The expression and purification of SpyCatcher-RBD (residues 319–541, prototype) from HEK-293 cells were completed by AtaGenix Laboratories Co., Ltd. (Wuhan, China.). Briefly, the 8 × His-labelled SpyCatcher-RBD DNA sequence (Supplementary Fig. 2a) was cloned into the pATX2 vector and transfected into HEK-293 cells. After 7 days, the culture medium soluble fraction was collected, and the His-labelled target proteins were purified by Ni-NTA affinity, and then concentrated after elution with Tris-buffer containing imidazole. The purified His-labelled proteins were identified by Coomassie blue staining and western blot analysis. The protein concentration was determined by the BCA method. His-labelled Omicron RBD (residues 319-541, B.1.1.529) (His-Omicron RBD) and His-labelled RBD proteins of different variants were obtained using a similar method.

ICO folding and purification

ICO design (115.5 bp edge length) was performed using the algorithmic framework software, DAEDALUS (http://daedalus-dna-origami.org). The sequence information of the staple strands for ICO fabrication are provided in Supplementary Data 1. The sequence information of the capture strands in the different ICO-RBD nanovaccines is also shown in Supplementary Data 1. DNA origami was fabricated by the following one-pot reaction: 20 nM M13mp18 scaffold was mixed with a 100 nM staple or capture strand mixture in 1 × TAE-Mg^{2+} buffer (40 mM Tris, 20 mM acetic acid, 2 mM EDTA, 12.5 mM $MgCl_2$, pH 8.0). The mixture was then self-assembled in a thermal cycler (T100, Bio-Rad) through the following program: 95 °C for 5 min, 80–75 °C at 1 °C per 5 min, 75–30 °C at 1 °C per 20 min and 30–25 °C at 1 °C per 10 min. The freshly prepared DNA origami was purified using 100 KDa MWCO centrifugal filters (Merck Millipore, UFC5100BK, USA) for 3 rounds to remove excess staple and capture strands. The concentration of the origami preparation was quantified using a NanoDrop 2000 (Thermo Fisher Scientific, USA) and stored at 4 °C for subsequent analysis. The origami was characterized by electrophoresis in a 0.6% agarose gel, and was imaged by TEM (JEM-1400) or AFM (Bruker, Multimode 8).

Antigen attachment to ICO

For SpyCatcher-RBD (prototype) protein attachment, SpyTag-N3 and DBCO-polyT were mixed at a molar ratio of 1:1, and reacted overnight at 4 °C to obtain SpyTag-polyT conjugates. Purified ICO was mixed with SpyTag-polyT conjugates at a molar ratio of 5:1 of poly T: polyA on the ICO. PolyT-polyA hybridization was performed by the following thermal cycler program: 45–25 °C at 1 °C per 5 min for 5 cycles, and a hold at 4 °C. The products (ICO-SpyTag) were purified using 100 KDa MWCO centrifugal filters (Merck Millipore, UFC5100BK) for 3 rounds to remove excess SpyTag-polyT conjugates. SpyCatcher-RBD proteins were then added to ICO-SpyTag at a molar ratio of 3:1 of SpyCatcher: SpyTag. This mixture was incubated at room temperature for 3 h, and excess Spycatcher-RBD proteins were removed by ultrafiltration.

For His-Omicron RBD attachment, NH_2-PolyT (100 μM) and NTA-PEG_{1000}-NHS (3 mM) were shaken at 25 °C, 400 rpm for 2 h. The pre-cooled ethanol (90%) and potassium acetate (pH5.5, 60 μM) were mixed, and left at −80 °C for 30 min, then 14000 *g* and centrifuged at 4 °C for 30 min. The supernatant was removed. After re-suspension with 100 μL PBS (pH7.4), the above ethanol precipitation steps were repeated. The supernatant was discarded and dried, and the obtained NTA-polyT was dissolved by TE Buffer for subsequent use. Purified ICO was mixed with NTA-polyT conjugates at a molar ratio of 5:1 of polyT: polyA on the ICO. PolyT-polyA hybridization was performed by the following thermal cycler program: 45–25 °C at 1 °C per 5 min for 5 cycles, and a hold at 4 °C. The products (ICO-NTA) were purified using

100 KDa MWCO centrifugal filters (Merck Millipore, UFC5100BK, USA) for 3 rounds to remove excess NTA-polyT conjugates. His-Omicron RBD proteins were then added to ICO-NTA at a molar ratio of 3:1 of His: NTA. This mixture was incubated at room temperature for 2 h, and excess His-Omicron RBD proteins were removed by ultrafiltration.

Protein quantification of ICO coverage with antigen

The antigen loading efficiency was quantified by ratio absorbance measurement. Specifically, the concentration of the DNA origami was measured by absorbance using a NanoDrop 2000 spectrophotometer at 260 nm, and the extinction coefficient of $10.9 \times 10^7 M^{-1} cm^{-1}$ was used for the calculation. The concentration of antigens was quantitatively determined using the BCA standard curve method. The antigen loading efficiency was defined as the percentage of measured protein concentration in nanovaccines compared to the theoretical concentration in the nanovaccines. At least 3 independent experiments were performed.

Preparation of mRNA vaccines

mRNA was synthesized through in vitro transcription using the HiScribe T7 mRNA Kit with CleanCap Reagent AG (NEB, China, Cat: E2080S). The templates for in vitro transcription were linearized plasmids, containing a T7 promoter, 5′-end UTR, signal peptide, Omicron RBD (residues 319-541, B.1.1.529), linker, T4 fibritin foldon trimerization domain, stop codon, 3′-end UTR and 120 polyA tail. The production of lipid nanoparticles was carried out using the NanoAssemblr Benchtop microfluid system (Precision NanoSystems, Canada). The lipid nanoparticle formulation was same as that of BNT162b2: ALC-0315: DSPC: Cholesterol: ALC-0159 = 46.3: 9.4: 42.7: 1.6.

Generation of B-RBD cells

Ramos B cells were obtained from Cell Resource Center, Institute of Basic Medicine, Chinese Academy of Medical Sciences, and were authenticated by the short tandem repeat analysis method and tested negative for mycoplasma contamination. The expression plasmid pRRL EuB29 COVA2-15 IgGTM. BCR. GFP. WPRE and the packaging plasmid mix (pMDL: pVSV-g: pRSV-Rev = 5: 3: 2) were co-transfected into HEK-293T cells at a ratio of 1:1 using lipofectamine 3000 (Invitrogen, USA, Cat: #L3000015). After 48 h, the supernatant from the cells was collected and filtered (0.45 μm), and then 50 μL of the concentrated viral supernatant was added to pre-plated Ramos B cells in 6-well plates (2×10^6 cells/well). After 7 days of transfection, the GFP^+IgG^+ cell population (B-RBD cells) were sorted by FACS (BD Aria III).

B cell binding assay

B-RBD cells were grown in RPMI 1640 medium (Gibco, Cat: #C11875500CP) supplemented with 10% fetal bovine serum (Gibco, Cat: #10091148) and 100 U/mL penicillin G sodium and 100 μg/mL streptomycin (Biological Industries, Cat: #03-031-1B). Cells (1×10^6) were harvested, suspended in PBS and incubated with 0.5 μg/mL SpyCatcher-RBD proteins or different ICO-RBD nanovaccine formulations at the same protein concentration for 1, 2, 4, 6, 8 or 10 min at 4 °C. Next, the cells were washed three times in PBS and incubated with anti-His antibodies at 4 °C for 40 min. The cells were then washed twice with PBS and SpyCatcher-RBD proteins or ICO-RBD nanovaccines bound to B-RBD cells were detected by flow cytometry. The gating strategies for flow cytometry analysis are shown in Supplementary Fig. 16.

B cell activation assay

B-RBD cells (1×10^7 cells/mL) were combined with 4 μM Fluo-4 AM (Invitrogen, USA, Cat: #F14217) for 20 min at 37 °C. The cells were then washed twice with HBSS (Solarbio, China, Cat: #H1025) and then incubated at 37 °C for 30 min. The washed cells were resuspended in PBS, and the nanovaccine-induced intracellular calcium changes were detected by flow cytometry (excitation/emission: 495 nm/518 nm). After a 35 s fluorescence baseline recording, 50 μL SpyCatcher-RBD proteins or ICO-RBD nanovaccines (5 μg/mL RBD) were added to the cells at 2×10^6 cells/mL and the fluorescence values were monitored for 3–5 min. The fluorescence value of a 50 μL PBS sample was used as a normalization standard at every time point.

Animal vaccination

All animal experiments were performed in accordance with animal use protocols approved by the Committee for the Ethics of Animal Experiments, the Institutional Animal Care and Use Committee of the National Center for Nanoscience and Technology. Mice were housed at 20–22 °C with a 12 h light/dark cycle and at 30–70% humidity. Female BALB/c mice (6 weeks old) were obtained from Charles River Laboratory Animal Technology Co. Ltd (Beijing, China).

For prototype RBD vaccine evaluation, six-week-old female BALB/c mice were randomly divided into 8 groups: PBS (control), ICO, RBD (SpyCatcher-RBD proteins), ICO + RBD (physical mixture), ICO-RBD-1c × 5–10 nm, ICO-RBD-1c × 5–40 nm, ICO-RBD-6c × 1–10 nm and ICO-RBD-6c × 5–10 nm. BALB/c mice were intramuscularly immunized with two doses of 50 μL nanovaccines containing 1 μg SpyCatcher-RBD at week 0 and 3, mixed with 50 μL AddaVax (InvivoGen, USA, Cat: #vac-adx-10). Serum samples were collected at week 2, 5, 8, 11 and 14, and RBD-specific IgG titers were measured by ELISA. Serum collected at week 5 and 14 was analyzed using a pseudovirus neutralization test. Spleens and lungs of mice were harvested at week 3 and 6 for T cell analysis. All mice were euthanized at week 14 and memory immune cells were evaluated.

For comparison of ICO-RBD nanovaccines and trimeric mRNA vaccines containing Omicron RBD, mice were randomly divided into 4 groups: PBS (control), RBD_{omic}, mRNA-RBD_{omic} and ICO-RBD_{omic}. The RBD_{omic} and ICO-RBD_{omic} vaccines contained 2 μg His-Omicron RBD proteins, and the mRNA-RBD_{omic} vaccines contained 10 μg mRNA. Mice were intramuscularly immunized with two doses of 50 μL vaccines at week 0 and 3, mixed with 50 μL AddaVax (only for RBD_{omic} and ICO-RBD_{omic} vaccines). Serum samples were collected at week 2 and 5, and RBD-specific IgG titers were measured by ELISA. Spleens and lungs of mice were harvested at week 6 for T cell analysis. All mice were euthanized at week 14 and memory immune cells were evaluated.

ELISA

SpyCatcher-RBD (prototype), His-Omicron RBD proteins or different RBD proteins of variants were diluted to 5 μg/mL with ELISA coating buffer (Solarbio, Cat: #C1055) and used to coat 96-well ELISA plates (Thermo Fisher, USA, Cat: #442404) at 4 °C overnight. The washed plates were blocked with 5% skim milk in PBS for 2 h. The serum was serially diluted and added to each well, and incubated at room temperature for 2 h. After washing the plates 3 times with PBS containing 1% Tween-20 (PBST), a goat anti-mouse IgG HRP antibody (Proteintech, USA, Cat: #SA00001-1) was diluted 1: 5000 in 5% skim milk, and added to the plates, which were then incubated at 37 °C for 1 h. After washing with PBST, the plates were developed with 3,3′,5,5′-tetramethylbenzidine (TMB; Solarbio, Cat: #PR1200). The color reaction was stopped using ELISA stop solution (Solarbio, Cat: #C1058), and the absorbance at 450 nm was read in a microplate reader (BioTEK, USA, Synergy H1). The data were analyzed by nonlinear regression to calculate the endpoint titer.

Pseudovirus neutralization assay

The pseudovirus neutralization assay was performed according to the manufacturer's instructions. Briefly, the serum samples and positive control (ACE2-Fc proteins) were diluted in a continuous gradient, and then mixed with resuscitated SARS-CoV-2 pseudovirus in a volume of 1: 1 at room temperature for 1 h, where the virus titer was 3×10^4 $TCID_{50}$/

mL. The mixture was added to HEK-293 cells expressing hACE2 (6×10^5/mL) and incubated in a 5% CO_2 incubator at 37 °C for 48 h. Luciferase activity was analyzed with a Luciferase Assay System (GenScript, Cat: #L00877C). The relative luminous unit (RLU) was standardized to the relative luminous unit of SARS-CoV-2 pseudovirus-infected cells in the absence of serum. Neutralization titer (ID_{50} value) was calculated as the serum dilution with 50% inhibition of infectivity.

Memory T cells, antigen-specific MBCs and LLPCs analysis

Splenocytes of mice were obtained and prepared as a single-cell suspension at week 14. For RBD-specific MBC analysis, Cy5.5-SpyTag was conjugated to SpyCatcher-RBD proteins to prepare “Cy5.5-RBD” fluorescent probes. Cells were incubated with Cy5.5-RBD for 1 h at 4 °C, washed 3 times with PBS, and then fixed and permeabilized. B220, IgG and CD38 antibodies were used to analyze antigen-specific MBCs in the splenocytes. The gating strategy for the flow cytometry analysis is shown in Supplementary Fig. 17. For LLPC analysis, splenocytes and bone marrow cells (from the femur and tibia) were obtained, and red blood cells were removed, to obtain single-cell suspensions. FITC-RBD probes were prepared according to the above method. Cells were stained with a mixture of B220, CD138, EpCAM and CXCR3 antibodies for 30 mins in 4 °C, and then washed 3 times with PBS. The cells were fixed and permeabilized by using the FOXP3 Fix/Perm buffer (BioLegend, Cat: # 421403). FITC-RBD was used for intracellular staining, and then washed with permeabilized buffer. The gating strategy for the flow cytometry analysis is shown in Supplementary Fig. 18. The central memory T cells and effector memory T cells in splenocytes were analyzed by flow cytometry after staining with CD3, CD8, CD44 and CD62L antibodies. The gating strategy for the flow cytometry analysis is shown in Supplementary Fig. 19.

Intracellular cytokine staining assays and TRMs analysis

Spleens and lungs of mice were harvested at week 3 and 6. The spleens were ground and passed through a 40 µm cell strainer to obtain single cell suspensions. The lungs were cut into pieces and treated with freshly prepared digestion buffer (0.05% trypsin solution, 1 mg/mL DNase and 1 mg/mL collagenase D) for 30 min with shaking at 120 rpm in 37 °C. The cells were stimulated with SpyCatcher-RBD or His-Omicron RBD proteins overnight, and then the cells were collected and stained with CD3, CD4 and CD8 antibodies. Fixation and permeabilization were performed after surface marker staining, and the cells were sequentially stained with IFN-γ, IL-2, TNF-α and IL-4 antibodies. The proportion of IFN-γ^+, IL-2^+, TNF-α^+ and IL-4^+ cells in $CD3^+CD8^+$ T cells and $CD3^+CD4^+$ T cells were analyzed using flow cytometry. The gating strategies for the flow cytometry analysis are shown in Supplementary Figs. 20 and 21. TRMs in the lung were analyzed after staining with CD8, CD69 and CD103 antibodies. The gating strategies for the flow cytometry analysis are shown in Supplementary Fig. 22.

DC and macrophage studies

Six-week-old female BALB/c mice were intramuscularly immunized with 50 µL Cy5.5-labelled SpyCatcher-RBD proteins or Cy5.5-labelled nanovaccines containing 1 µg SpyCatcher-RBD proteins, mixed with 50 µL AddaVax. After different time, the inguinal lymph nodes were obtained and then fluorescence imaging was performed. Single cell suspensions were obtained after grinding the samples. The $Cy5.5^+$ cells in DCs ($CD11C^+$), resident DCs ($CD103^-CD11C^+$), migrated DCs ($CD103^+CD11C^+$), follicular DCs ($CD21/CD35^+CD11C^+$), mature DCs ($CD11C^+CD80^+$, $CD11C^+CD86^+$) and macrophages ($F4/80^+$) were analyzed using flow cytometry. The gating strategies for the flow cytometry analysis are shown in Supplementary Fig. 23. The inguinal lymph nodes were also collected on day 1 and 3, and the cryosections were cut to perform immunofluorescent staining.

Analysis of GC B, T_{FH} and plasma cells

For GC B cells and T_{FH} cell response analysis, six-week-old female BALB/c mice were randomly divided into 3 groups: PBS, RBD (SpyCatcher-RBD proteins) and ICO-RBD nanovaccines. After priming immunization, the inguinal lymph nodes were harvested at week 1, 2 and 3. Single cell suspensions were then obtained by grinding and sieving the nodes. Next, the percentages of GC B cells ($CD19^+B220^+CD95^+GL7^+$), T_{FH} cells ($CD4^+CXCR5^+PD\text{-}1^+$) and plasma cells ($CD44^+CD138^+$) were analyzed by flow cytometry. The gating strategies for the flow cytometry analysis are shown in Supplementary Fig. 24. The inguinal lymph nodes were also collected on week 1, and the cryosections were cut to perform immunofluorescent staining.

Culture of BMDCs

Briefly, bone marrow cells were flushed from the femurs and tibias of mice and cultured in RPMI 1640 supplemented with 10% FBS, 100 U/mL penicillin G sodium, 100 µg/mL streptomycin, 1% HEPES, 0.05 mM β-mercaptoethanol (β-ME), 20 ng/mL IL-4 (Cell Signaling Technology, USA, Cat: 5208SC) and 20 ng/mL GM-CSF (PeproTech, USA, Cat: 315-03-20UG), after lysed the red blood cells using ACK Lysis Buffer (Solarbio, China, Cat: R1010) to induce differentiation into immature BMDCs.

Protection of vaccines against SARS-CoV-2

The animal infection experiment was conducted in the ABSL-3 Laboratory of Changchun Veterinary Research Institute, Chinese Academy of Agricultural Sciences. The hamster experiments protocol was approved by the Institutional Animal Care and Use Committee of Beijing Institute of Biotechnology (code IACUC-SWGCYJS-2023-010). Hamsters were randomly divided into 3 groups and were priming- and boost-vaccinated with the indicated vaccines containing 1 µg prototype RBD at week 0 and 3, respectively. Two weeks post boost, hamsters were challenged with authentic SARS-CoV-2 (WH-01 strain). Each hamster was infected with 10^4 TCID50 viral particles (WH-01 strain) through the intranasal route. Nasal washes were collected at day 2, 4, and 6 post challenge, The nasal of these hamsters was washed twice using 1 mL of PBS, and total RNA was extracted from the 200 µL of recovered fluid. Hamsters were euthanized and lung tissue were collected at day 7 post challenge, and 1 mL of PBS was added to the lung tissue and thoroughly homogenized. 200 µL of the homogenized suspension was used for the extraction of total RNA. All the RNA extractions were performed on TGuide S96 Automated Nucleic Acid Extractor (YOSE-S96, Tiangen, Beijing, China) using TGuide S96 Magnetic Viral DNA/ RNA Kit (CDP804, Tiangen, Beijing, China). Viral load was quantified from the total RNA extracts by qPCR targeting the nucleocapsid (N) gene and normalized by hamster GAPDH. N gene was quantified using the SARS-CoV-2 N Gene Probe qRT-PCR Kit (15-81920 y, Tiandz, Beijing, China). The golden hamster constitutive gene GAPDH was used as the endogenous control to standardized the N gene RT-qPCR copy numbers. Primers were as follows: Forward, 5′-GTG GAGCCAAGAGGGTCATC-3′; reverse, 5′-GGTTCACACCCATCACAAA CAT-3. 5′-FAM-TCTCCGCACCTTCTGCTGATGCC-3′-TAMRA (GenBank accession no. DQ403055.1) is the probe used in this experiment. FAM is 6-carboxyfluorescein and TAMRA is 6-carboxytetramethylrhodamine. The viral load was calculated by the (N gene RT-qPCR copy numbers/ hamster genome mass equivalents) ratio and expressed as “viral load” (SARS-CoV-2 RNA copies/ng genome equivalent).

Statistical analysis

Details on the statistical analysis for the experiments, including the number of samples, mean ± standard errors of the mean (SEM) or mean ± standard deviation (SD) are shown in the figure legends. Statistical analysis was performed using Prism 8 (GraphPad) on data pooled from at least 3 independent experiments. For multiple-group comparisons, one-way ANOVA followed by Tukey’s test, was applied.

For two-group viral RNA copies comparisons were calculated by a two-tailed unpaired *t* test.

Reporting summary

Further information on research design is available in the Nature Portfolio Reporting Summary linked to this article.

Data availability

The main data supporting the results in this study are available within the paper and its Supplementary Information/Data. There are no data from third-party or publicly available datasets. Other source data that support the findings of this study are available from the corresponding authors upon reasonable request. Source data are provided with this paper.

References

1. V'Kovski, P., Kratzel, A., Steiner, S., Stalder, H. & Thiel, V. Coronavirus biology and replication: implications for SARS-CoV-2. *Nat. Rev. Microbiol.* **19**, 155–170 (2021).
2. Dai, L. & Gao, G. F. Viral targets for vaccines against COVID-19. *Nat. Rev. Immunol.* **21**, 73–82 (2021).
3. van Riel, D. & de Wit, E. Next-generation vaccine platforms for COVID-19. *Nat. Mater.* **19**, 810–812 (2020).
4. Zhu, F. C. et al. Immunogenicity and safety of a recombinant adenovirus type-5-vectored COVID-19 vaccine in healthy adults aged 18 years or older: a randomised, double-blind, placebo-controlled, phase 2 trial. *Lancet (Lond., Engl.)* **396**, 479–488 (2020).
5. Keech, C. et al. Phase 1-2 Trial of a SARS-CoV-2 Recombinant Spike Protein Nanoparticle Vaccine. *N. Engl. J. Med.* **383**, 2320–2332 (2020).
6. Dai, L. et al. A Universal Design of Betacoronavirus Vaccines against COVID-19, MERS, and SARS. *Cell* **182**, 722–733.e711 (2020).
7. Graham, B. S. Rapid COVID-19 vaccine development. *Science* **368**, 945–946 (2020).
8. Su, S., Du, L. & Jiang, S. Learning from the past: development of safe and effective COVID-19 vaccines. *Nat. Rev. Microbiol.* **19**, 211–219 (2021).
9. Wang, Q. et al. Immunodominant SARS Coronavirus Epitopes in Humans Elicited both Enhancing and Neutralizing Effects on Infection in Non-human Primates. *ACS Infect. Dis.* **2**, 361–376 (2016).
10. Yang, J. et al. A vaccine targeting the RBD of the S protein of SARS-CoV-2 induces protective immunity. *Nature* **586**, 572–577 (2020).
11. Zhang, N. N. et al. A Thermostable mRNA Vaccine against COVID-19. *Cell* **182**, 1271–1283.e1216 (2020).
12. Yang, S. et al. Safety and immunogenicity of a recombinant tandem-repeat dimeric RBD-based protein subunit vaccine (ZF2001) against COVID-19 in adults: two randomised, double-blind, placebo-controlled, phase 1 and 2 trials. *Lancet Infect. Dis.* **21**, 1107–1119 (2021).
13. Gu, H. et al. Adaptation of SARS-CoV-2 in BALB/c mice for testing vaccine efficacy. *Science* **369**, 1603–1607 (2020).
14. Liu, Z. et al. RBD-Fc-based COVID-19 vaccine candidate induces highly potent SARS-CoV-2 neutralizing antibody response. *Signal Transduct. Target. Ther.* **5**, 282 (2020).
15. Walsh, E. E. et al. Safety and Immunogenicity of Two RNA-Based Covid-19 Vaccine Candidates. *N. Engl. J. Med.* **383**, 2439–2450 (2020).
16. Mulligan, M. J. et al. Phase I/II study of COVID-19 RNA vaccine BNT162b1 in adults. *Nature* **586**, 589–593 (2020).
17. Ma, X. et al. Nanoparticle Vaccines Based on the Receptor Binding Domain (RBD) and Heptad Repeat (HR) of SARS-CoV-2 Elicit Robust Protective Immune Responses. *Immunity* **53**, 1315–1330.e1319 (2020).
18. Cohen, A. A. et al. Mosaic nanoparticles elicit cross-reactive immune responses to zoonotic coronaviruses in mice. *Science* **371**, 735–741 (2021).
19. Arunachalam, P. S. et al. Adjuvanting a subunit COVID-19 vaccine to induce protective immunity. *Nature* **594**, 253–258 (2021).
20. Kanekiyo, M. et al. Self-assembling influenza nanoparticle vaccines elicit broadly neutralizing H1N1 antibodies. *Nature* **499**, 102–106 (2013).
21. Boyoglu-Barnum, S. et al. Quadrivalent influenza nanoparticle vaccines induce broad protection. *Nature* **592**, 623–628 (2021).
22. Tan, T. K. et al. A COVID-19 vaccine candidate using SpyCatcher multimerization of the SARS-CoV-2 spike protein receptor-binding domain induces potent neutralising antibody responses. *Nat. Commun.* **12**, 542 (2021).
23. Ke, Z. et al. Structures and distributions of SARS-CoV-2 spike proteins on intact virions. *Nature* **588**, 498–502 (2020).
24. Saccà, B. & Niemeyer, C. M. DNA origami: the art of folding DNA. *Angew. Chem. (Int. ed. Engl.)* **51**, 58–66 (2012).
25. Hong, F., Zhang, F., Liu, Y. & Yan, H. DNA Origami: Scaffolds for Creating Higher Order Structures. *Chem. Rev.* **117**, 12584–12640 (2017).
26. Liu, S. et al. A DNA nanodevice-based vaccine for cancer immunotherapy. *Nat. Mater.* **20**, 421–430 (2021).
27. Kong, G. et al. DNA origami-based protein networks: from basic construction to emerging applications. *Chem. Soc. Rev.* **50**, 1846–1873 (2021).
28. Rosier, B. et al. Proximity-induced caspase-9 activation on a DNA origami-based synthetic apoptosome. *Nat. Catal.* **3**, 295–306 (2020).
29. Fang, T. et al. Spatial Regulation of T-Cell Signaling by Programmed Death-Ligand 1 on Wireframe DNA Origami Flat Sheets. *ACS Nano* **15**, 3441–3452 (2021).
30. Hellmeier, J., et al. DNA origami demonstrate the unique stimulatory power of single pMHCs as T cell antigens. *Proc. Natl. Academy Sci. USA* **118**, e2016857118 (2021).
31. Veneziano, R. et al. Role of nanoscale antigen organization on B-cell activation probed using DNA origami. *Nat. Nanotechnol.* **15**, 716–723 (2020).
32. Feng, Q. et al. Deficiency of miRNA-149-3p shaped gut microbiota and enhanced dextran sulfate sodium-induced colitis. *Mol. Ther. Nucleic acids* **30**, 208–225 (2022).
33. Wamhoff, E. C. et al. Enhancing antibody responses by multivalent antigen display on thymus-independent DNA origami scaffolds. *Nat. Commun.* **15**, 795 (2024).
34. Oktay, E. et al. DNA origami presenting the receptor binding domain of SARS-CoV-2 elicit robust protective immune response. *Commun. Biol.* **6**, 308 (2023).
35. Zakeri, B. et al. Peptide tag forming a rapid covalent bond to a protein, through engineering a bacterial adhesin. *Proc. Natl. Acad. Sci. USA* **109**, E690–E697 (2012).
36. Zhang, Y. N. et al. Nanoparticle Size Influences Antigen Retention and Presentation in Lymph Node Follicles for Humoral Immunity. *Nano Lett.* **19**, 7226–7235 (2019).
37. Brouwer, P. J. M. et al. Two-component spike nanoparticle vaccine protects macaques from SARS-CoV-2 infection. *Cell* **184**, 1188–1200.e1119 (2021).
38. Brouwer, P. J. M. et al. Potent neutralizing antibodies from COVID-19 patients define multiple targets of vulnerability. *Science* **369**, 643–650 (2020).
39. Akkaya, M., Kwak, K. & Pierce, S. K. B cell memory: building two walls of protection against pathogens. *Nat. Rev. Immunol.* **20**, 229–238 (2020).
40. Liu, X., Yao, J., Zhao, Y., Wang, J. & Qi, H. Heterogeneous plasma cells and long-lived subsets in response to immunization, autoantigen and microbiota. *Nat. Immunol.* **23**, 1564–1576 (2022).
41. Ols, S., et al. Multivalent antigen display on nanoparticle immunogens increases B cell clonotype diversity and neutralization breadth to pneumoviruses. *Immunity* **56**, 2425–2441 (2023).

42. Jiang, S. et al. Identification of a promiscuous conserved CTL epitope within the SARS-CoV-2 spike protein. *Emerg. Microbes Infect.* **11**, 730–740 (2022).
43. Tarke, A. et al. SARS-CoV-2 vaccination induces immunological T cell memory able to cross-recognize variants from Alpha to Omicron. *Cell* **185**, 847–859.e811 (2022).
44. Schenkel, J. M. et al. T cell memory. Resident memory CD8 T cells trigger protective innate and adaptive immune responses. *Science* **346**, 98–101 (2014).
45. Rappuoli, R. Glycoconjugate vaccines: Principles and mechanisms. *Sci. Transl. Med.* **10**, eaat4615 (2018).
46. Kelly, H. G., et al. Self-assembling influenza nanoparticle vaccines drive extended germinal center activity and memory B cell maturation. *JCI insight* **5**, e136653 (2020).
47. Moreira, E. D. Jr. et al. Safety and Efficacy of a Third Dose of BNT162b2 Covid-19 Vaccine. *N. Engl. J. Med.* **386**, 1910–1921 (2022).

Acknowledgements

This work was supported by grants from the Beijing Municipal Science & Technology Commission (Z231100007223011), National Key R&D Program of China (2022YFB3808100 and 2021YFA0909900, X.Z.), Strategic Priority Research Program of Chinese Academy of Sciences (XDB36000000, G.N.), the CAS Project for Young Scientists in Basic Research (YSBR-010, X.Z.), the Beijing Natural Science Foundation (Z200020, X.Z.) and the National Natural Science Foundation of China (32222045 and 32171384, X.Z.).

Author contributions

Q.F., K.C., L.Z. and D.W. contributed equally to this work. Q. F. and X.Z. designed the research. Q. F., K.C., L.Z., X.G., J.L., G.L., N.M., C.X., M.T., L.C., X.W., X.M., J.Z., Q. S.P.D., and Q.W. performed the research. All authors analyzed and interpreted the data. D. W. and H. W. were mainly responsible for the protection experiments from authentic SARS-CoV-2. Q.F., G.N. and X.Z. wrote the paper. G.N. and X.Z. conceived and supervised the project.

Competing interests

Q.F., J.Z., Q.S. and X.Z. are inventors on a filed provisional application of Chinese patent (Nano-assembly of antigens based on DNA origami and the application in vaccine) submitted by the National Center for Nanoscience and Technology and Beijing Intell Nanomedicine that covers the potential diagnostic and therapeutic uses of DNA-antigen complex. The authors declare that they have no other competing interests.

Additional information

Supplementary information The online version contains supplementary material available at https://doi.org/10.1038/s41467-024-53937-4.

Correspondence and requests for materials should be addressed to Hengliang Wang, Guangjun Nie or Xiao Zhao.

Peer review information *Nature Communications* thanks Xing Wang, who co-reviewed with Abhisek Dwivedy, Pascal Chappert and the other, anonymous, reviewer(s) for their contribution to the peer review of this work. A peer review file is available.

Reprints and permissions information is available at http://www.nature.com/reprints

Publisher's note Springer Nature remains neutral with regard to jurisdictional claims in published maps and institutional affiliations.

Open Access This article is licensed under a Creative Commons Attribution-NonCommercial-NoDerivatives 4.0 International License, which permits any non-commercial use, sharing, distribution and reproduction in any medium or format, as long as you give appropriate credit to the original author(s) and the source, provide a link to the Creative Commons licence, and indicate if you modified the licensed material. You do not have permission under this licence to share adapted material derived from this article or parts of it. The images or other third party material in this article are included in the article's Creative Commons licence, unless indicated otherwise in a credit line to the material. If material is not included in the article's Creative Commons licence and your intended use is not permitted by statutory regulation or exceeds the permitted use, you will need to obtain permission directly from the copyright holder. To view a copy of this licence, visit http://creativecommons.org/licenses/by-nc-nd/4.0/.

© The Author(s) 2024

---

[1]CAS Key Laboratory for Biomedical Effects of Nanomaterials and Nanosafety & CAS Center for Excellence in Nanoscience, National Center for Nanoscience and Technology of China, 11 Beiyitiao, Zhongguancun, Beijing 100190, China. [2]Center of Materials Science and Optoelectronics Engineering, University of Chinese Academy of Sciences, Beijing 100049, China. [3]IGDB-NCNST Joint Research Center, Institute of Genetics and Developmental Biology, Chinese Academy of Sciences, Beijing 100101, China. [4]State Key Laboratory of Pathogens and Biosecurity, Laboratory of Advanced Biotechnology, Beijing Institute of Biotechnology, 20 Dongdajie Street, Fengtai District, Beijing 100071, China. [5]CAS Key Laboratory of Pathogen Microbiology and Immunology, Institute of Microbiology, Chinese Academy of Sciences, NO.1 Beichen West Road, Chaoyang District, Beijing 100101, China. [6]Beijing Intell Nanomedicine, No. 9, Chengwan Street, Haidian District, Beijing 100000, China. [7]These authors contributed equally: Qingqing Feng, Keman Cheng, Lizhuo Zhang, Dongshu Wang. ✉e-mail: wanghl@bmi.ac.cn; niegj@nanoctr.cn; zhaox@nanoctr.cn